

CZECH TECHNICAL UNIVERSITY  
IN PRAGUE

Faculty of Nuclear Sciences and Physical  
Engineering

Department of Physics



## Research project

Mass composition, energy spectrum  
and propagation of ultra-high energy  
cosmic rays

Bc. Alena Bakalová

Supervisor: Ing. Jakub Vicha, Ph.D.

Prague, 2017



ČESKÉ VYSOKÉ UČENÍ TECHNICKÉ  
V PRAZE

Fakulta jaderná a fyzikálně inženýrská

Katedra fyziky



## Výzkumný úkol

**Složení, energetické spektrum a  
propagace kosmického záření ultra  
vysokých energií**

**Bc. Alena Bakalová**

**Školitel: Ing. Jakub Vícha, Ph.D.**

**Praha, 2017**



**Prohlášení:**

Prohlašuji, že jsem svůj výzkumný úkol vypracovala samostatně a použila jsem pouze podklady (literaturu, projekty, SW atd.) uvedené v příloženém seznamu.

Nemám závažný důvod proti použití tohoto školního díla ve smyslu § 60 Zákona č. 121/2000 Sb., o právu autorském, o právech souvisejících s právem autorským a o změně některých zákonů (autorský zákon).

V Praze dne

Alena Bakalová



*Title:*

**Mass composition, energy spectrum and propagation of ultra-high energy cosmic rays**

*Author:* Alena Bakalová

*Specialization:* Experimental nuclear and particle physics

*Supervisor:* Ing. Jakub Vícha, Ph.D.

---

*Abstract:*

The origin of cosmic-ray particles of ultra-high energies is still unknown and is a subject of current research. Cosmic-ray particles propagating through the Universe are losing their energy and being subjected to nuclear transformation due to photodisintegration of nucleus on ambient photons. Measuring cosmic ray shower secondary particles induced in the Earth's atmosphere we are able to reconstruct the maximum of the shower development that is sensitive to the mass composition of the primary particles. Interpretation of recent data from fluorescence detectors indicates that at the highest energies the combined mass spectrum of primary particles shifts towards higher nuclear mass numbers. We present an application of the reconstruction of the surface detector data of the Pierre Auger Observatory using shower universality together with the results from simulations concerning the propagation of cosmic rays in the Universe performed in CRPropa 3.

*Key words:* Ultra-High Energy Cosmic Rays, Mass Composition of Cosmic Rays, Shower Universality, Propagation of Cosmic Rays, CRPropa.



*Název:*

**Složení, energetické spektrum a propagace kosmického záření ultra-vysokých energií**

*Autor:* Alena Bakalová

*Obor:* Experimentální jaderná a částicová fyzika

*Školitel:* Ing. Jakub Vícha, Ph.D.

---

*Abstrakt:*

Původ částic kosmického záření ultra vysokých energií je stále nezodpovězenou otázkou astročásticové fyziky a je předmětem současného výzkumu. Částice kosmického záření během své propagace vesmírem ztrácejí energii a mohou také podléhat jaderným transformacím, které jsou způsobeny fotodezintegrací na fotonech přítomných v kosmickém prostoru. Kosmické záření dopadající do zemské atmosféry vytváří rozsáhle spršky sekundárních částic. Jejich detekci fluorescenčními teleskopy jsme schopni zrekonstruovat maximum spršky, které je citlivé na typ primární částice. Současné interpretace měření ukazují posun hmotnostního složení kosmického záření nejvyšších energií směrem k těžším primárním prvkům. V této práci uvádíme výsledky rekonstrukce dat naměřených povrchovými detektory Observatoře Pierra Augera pomocí univerzality spršek. Dále jsou zde prezentovány výsledky simulací zabývajících se propagací kosmického záření vesmírem provedených v programu CRPropa 3.

*Klíčová slova:* kosmické záření ultra vysokých energií, složení kosmického záření, univerzalita spršek, propagace kosmického záření, CRPropa.



## **Acknowledgement**

I would like to thank my supervisor, Ing. Jakub Vícha, Ph.D. for his patience, professional mentoring and valuable help and comments regarding this research project.



# Contents

|          |                                                         |           |
|----------|---------------------------------------------------------|-----------|
| <b>1</b> | <b>Cosmic Rays</b>                                      | <b>12</b> |
| 1.1      | Energy Spectrum . . . . .                               | 12        |
| 1.2      | Mass Composition . . . . .                              | 13        |
| 1.3      | Energy Losses . . . . .                                 | 16        |
| 1.3.1    | Photo-pion Production . . . . .                         | 16        |
| 1.3.2    | Photodisintegration of Nuclei . . . . .                 | 17        |
| 1.3.3    | Pair Production . . . . .                               | 17        |
| 1.3.4    | Expansion of the Universe . . . . .                     | 18        |
| <b>2</b> | <b>The Pierre Auger Observatory</b>                     | <b>20</b> |
| 2.1      | Observatory Design . . . . .                            | 20        |
| 2.1.1    | Surface Detectors . . . . .                             | 21        |
| 2.1.2    | Fluorescence Detectors . . . . .                        | 22        |
| 2.2      | Shower Reconstructions . . . . .                        | 22        |
| 2.2.1    | Hybrid Reconstruction . . . . .                         | 23        |
| 2.2.2    | SD Reconstruction . . . . .                             | 24        |
| 2.2.3    | Shower Universality Reconstruction . . . . .            | 25        |
| <b>3</b> | <b>Simulation of Propagation of Cosmic-ray</b>          | <b>27</b> |
| 3.1      | CRPropa . . . . .                                       | 27        |
| 3.2      | SimProp . . . . .                                       | 29        |
| <b>4</b> | <b>Results</b>                                          | <b>31</b> |
| 4.1      | Shower Maximum measured by the Pierre Auger Observatory | 31        |
| 4.2      | Simulated Propagation of Cosmic Rays . . . . .          | 36        |
| 4.2.1    | Propagation of Cosmic Rays in the Universe . . . . .    | 36        |
| 4.2.2    | Observation at the Earth . . . . .                      | 42        |
| <b>5</b> | <b>Conclusions</b>                                      | <b>50</b> |

# Introduction

It has been more than a hundred years since the discovery of cosmic rays and more than fifty years since the discovery of cosmic rays of ultra-high energies (above  $10^{18}$  eV). Despite such a long time, the origin and means of acceleration of the most energetic cosmic-ray particles still remain unanswered questions. A shower of secondary particles is created when the primary particle from the outer space hits atmospheric nuclei. The most energetic particles reaching the Earth have energy more than  $10^{20}$  eV, which in the centre of mass system corresponds to  $\approx 800$  TeV taking into account a collision of proton with the nucleus of the atmospheric nitrogen. Such energy is still unreachable even at the most modern current accelerator experiments. Therefore the properties of the first interactions (cross sections, elasticity, multiplicity etc.) taking place in the cosmic-ray shower are extrapolated to many orders of magnitude higher energies than the collision energies at the accelerator experiments. For that reason, there are high uncertainties in the interpretation of the air-shower measurements at the highest energies.

Since the energy spectrum of cosmic rays follows approximately  $E^{-3}$  the most energetic events are very rare, for more details see [1]. Therefore large-area observatories are constructed in order to study the cosmic-ray physics at ultra-high energies, such as the Pierre Auger Observatory in Argentina covering an area of  $3000 \text{ km}^2$  [2] or Telescope Array in the USA with detectors distributed across an area of  $762 \text{ km}^2$  [3]. These experiments sample the secondary particles reaching the ground and a reversed reconstruction is then needed to determine the energy, direction or the type of the primary particle. It is also possible to detect the fluorescence light emitted by nitrogen atoms during the shower development, which is proportional to the deposited energy in the atmosphere.

In this work, we will introduce results concerning propagation of cosmic-ray particles simulated in CRPropa 3. The main focus is given to the energy losses and change in the type of the nuclei due to the interactions with cosmic microwave background. In Chapter 1, the properties of cosmic rays are discussed with a more detailed focus on the their propagation in the

Universe. The apparatus of the Pierre Auger Observatory is described in the Chapter 2 together with algorithms used for shower reconstructions. The simulation of the cosmic-ray propagation in the Universe is introduced in the Chapter 3. The results relating the interpretation of data measured at the Pierre Auger Observatory and simulated propagation of cosmic rays are presented in Chapter 4 and finally summarized in the last chapter.

# Chapter 1

## Cosmic Rays

Cosmic rays were discovered by Victor Franz Hess [4] who undertook series of balloon ascents between 1911 and 1913 measuring the size of air ionization. During numerous flights he reached the maximum height of 5,350 m and from the measurements he concluded that the ionization of air increases with altitude above 1 km a.s.l., which implies that the radiation does not come from the Earth but rather from the space [4]. Cosmic rays are particles coming from outer space, mainly originating outside the Solar System. These particles, called primary particles of cosmic rays, are predominantly protons (86%), alpha particles (11%) and nuclei of heavier elements, such as nitrogen or iron [1]. A shower of secondary particles is created when a primary cosmic-ray particle hits and atmospheric nucleus. A wide range of particles can be created during the formation of cosmic ray shower including pions, kaons, muons, electrons, photons or neutrinos.

### 1.1 Energy Spectrum

The energy spectrum of cosmic rays is very wide and covers more than ten orders of magnitude with the number of incoming particles rapidly decreasing with increasing energy  $E$ . The dependency is falling approximately as  $E^{-3}$  as can be seen in Figure 1.1. The energy spectrum has three major features. A steepening of the spectrum, the so called "knee", occurs around the energy  $E \approx 10^{15.6}$  eV. Another significant change in the spectrum is its hardening around the energy  $E \approx 10^{18.6}$  eV referred to as the "ankle". Last important feature is the cut-off at the highest energies above  $E \approx 10^{19.6}$  eV [5]. Additional less visible feature is another knee around the energy  $E \approx 10^{17.5}$  eV [6, 7].

These changes of the spectral index of the energy spectrum are reflect-

ing mechanisms of cosmic ray production, such as the maximal rigidity of the sources or the Galactic magnetic confinement. The first knee is usually explained as an energy at which the galactic protons drop out because of the absence of sources capable of acceleration to higher energies. The second knee is observed at energies where the heaviest nuclei (i.e. up to iron) drop out [5]. The cut-off at the end of the energy spectrum was predicted by Greisen [8], Zatsepin and Kuzmin [9] who calculated a theoretical upper limit of the energy of cosmic-ray protons from distant sources which comes as a result of photopion production due to interactions with the cosmic microwave background ("CMB"). This energy is usually referred to as the GZK cut-off ( $E = 10^{19.7}$  eV) which is in nice agreement with the measurements of the Pierre Auger Observatory and HiRes (see Figure 1.1).

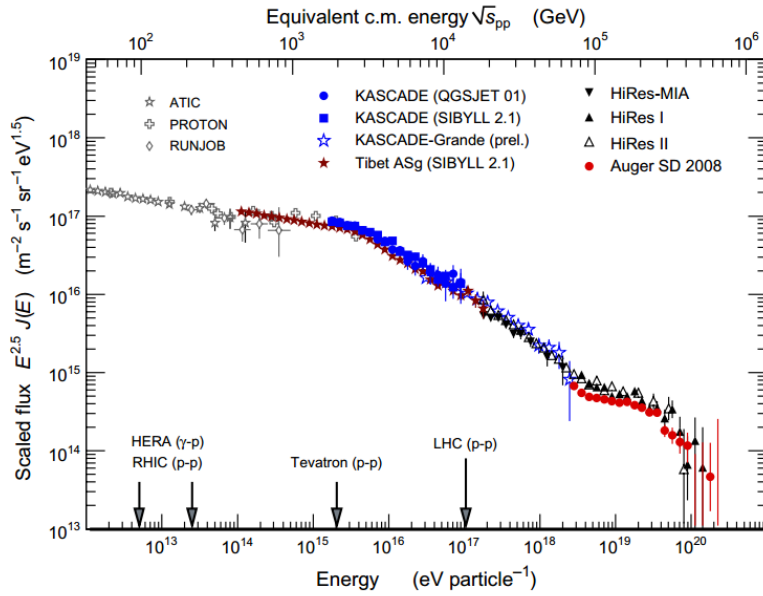


Figure 1.1: The energy spectrum of cosmic rays obtained from various experiments [10]. Note the flux scaling by energy  $E^{2.5}$ .

## 1.2 Mass Composition

The mass composition of primary cosmic rays evolves with energy. As it was already mentioned in the previous section, some of the important features of the energy spectrum are related to the rigidity of the sources or to the Galactic magnetic confinement which means that different nuclei will be dominant at different energies. A detailed knowledge of the chemical composition of

ultra-high energy cosmic rays ("UHECR") is a key factor to understand the physics of their origin and their propagation in the universe.

Since we are able to detect only the secondary particles of cosmic-ray showers and not the primary ones at the ultra-high energies we need to find shower properties that are sensitive to the chemical composition of the primary particle. The depth<sup>1</sup> of shower maximum ( $X_{\max}$ ) is one of the most sensitive quantities to the mass composition of primary particles. It can be reconstructed from the signal in fluorescence detectors that can not be operated at any time, but only when there is minimal background light implying low duty cycle ( $\sim 10\%$ ).  $X_{\max}$  is the depth in the atmosphere, where the shower contains the most electromagnetic particles. Predictions of  $X_{\max}$  and other shower parameters are made in simulations for a primary particle of given energy using different models of hadronic interactions, such as EPOS-LHC [11], QGSJetII-04 [12] or Sibyll 2.1 [13]. These predicted values of  $X_{\max}$  are used to determine the mass composition of primary particles that induced a real detected air shower. A small statistics at the highest energies is a severe problem for the interpretation of measured data. The use of surface detectors operating almost 100% of the time for the mass composition measurement is an ideal way to increase the statistics. For instance, it has been shown that the depth of production of muons ( $X_{\max}^{\mu}$ ) measured by surface detectors can be also used for mass composition analysis at higher zenith angles up to energies beyond  $6 \cdot 10^{19}$  eV [14]. Ongoing upgrade of the Pierre Auger Observatory is intended to improve the mass composition analysis based on surface detectors for all zenith angles.

Mean values of  $X_{\max}$  measured by the fluorescence detectors of the Pierre Auger Observatory are illustrated in Figure 1.2. The plot shows also predictions for the energy dependence of  $X_{\max}$  for protons and iron nuclei for different models of hadronic interactions. The data indicates that the mass composition becomes lighter in the region around the energy  $2 \cdot 10^{18}$  eV and at higher energies, the mass composition tends towards heavier primary particles.

The energy dependence of the mean  $\ln A$ , where  $A$  is the nucleon number, from  $X_{\max}$  and  $X_{\max}^{\mu}$  measurements based on predictions of EPOS-LHC and QGSJetII-04 are shown in Figure 1.3. Obviously, EPOS-LHC suggests non-physical conclusions based on  $X_{\max}^{\mu}$  predictions, since components heavier

---

<sup>1</sup>The atmospheric depth  $X$  at the altitude  $h$  is defined as

$$X = \int_{\infty}^h \frac{l \cdot \rho(l)}{\cos \theta} dl,$$

where  $\rho(l)$  is the density of air at altitude  $l$  and  $\theta$  is the zenith angle of primary particle.

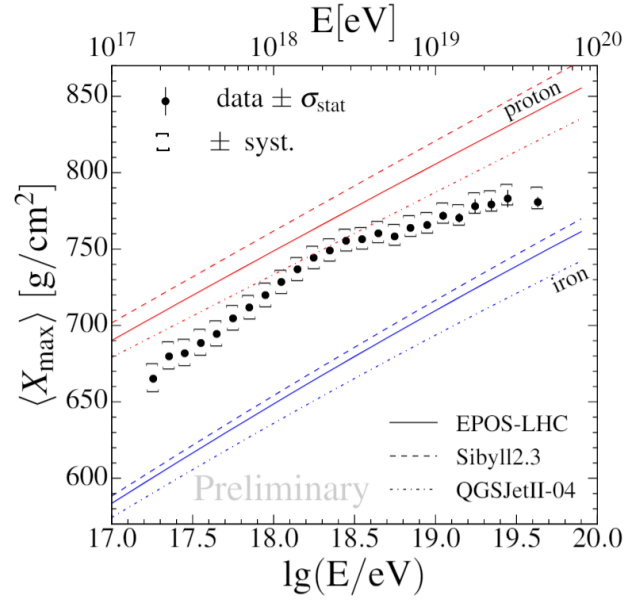


Figure 1.2: Energy dependence of the mean  $X_{\max}$  measured by fluorescence detectors of the Pierre Auger Observatory [15].

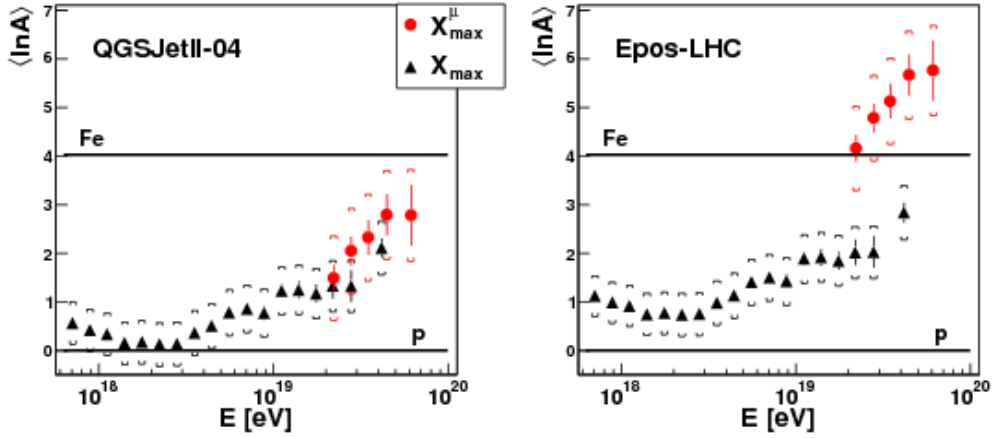


Figure 1.3: Energy dependence of the mean  $\ln A$  interpreted from  $X_{\max}$  (black) and  $X_{\max}^{\mu}$  (red) measurements at the Pierre Auger Observatory based on predictions by EPOS-LHC (right) and QGSJetII-04 (left) [14].

than iron are astrophysically improbable. Also this figure indicates that the average mass number is increasing with energy above  $2 \cdot 10^{18}$  eV, where the mass composition seems to be the lightest in the studied region.

## 1.3 Energy Losses

Large-area observatories are built to understand the basic properties of ultra-high energy cosmic rays, so that the questions about their origin can be answered. However, during propagation of UHECR from the source to the Earth the original energy spectrum and chemical composition produced by the source can be modified. This is a consequence of the interactions with low energy photons of CMB and extragalactic background light ("EBL"). That means that we need to understand the propagation effects very well to truly understand the physics behind the origin of UHECR. Moreover, direction of charged particles are also influenced by the magnetic field of our Galaxy and also by extragalactic magnetic fields.

The difference between the chemical composition of UHECR on Earth and at the sources depends on many factors. The most important variables are the distance of the source, the energy of primary particles, strength, direction and location of magnetic fields and the mean photon and energy density in the part of the Universe the particle is passing through.

The most important intergalactic medium is the cosmic microwave background radiation. This radiation is a remnant from an early stage of the Universe, called the recombination, when the Universe became transparent to photons. CMB follows the black-body radiation and has the temperature of  $\sim 2.7$  K corresponding to the mean energy of approximately  $10^{-3}$  eV with very low fluctuations of the temperature ( $\sim 10^{-5}$  K). Cosmic rays can also interact with optical, infra-red background radiation ("IBR") or radio waves. In the following, the most important energy losses of UHECR due to interactions with CMB and EBL will be described.

### 1.3.1 Photo-pion Production

A photo-pion production is one of the most significant losses at the highest energies. The production of a pion in a collision of nucleon  $N$  and background photon  $\gamma$  can be described as  $N + \gamma \rightarrow N + \pi$ . The threshold energy for this process is given by the equation

$$E_{thres}^{N,\pi} = \frac{m_\pi(m_N + \frac{1}{2}m_\pi)}{2\epsilon} \approx 6.8 \cdot 10^{19} \left( \frac{\epsilon}{10^{-3} \text{ eV}} \right)^{-1} \text{ eV}, \quad (1.1)$$

where  $m_\pi$  and  $m_N$  are the masses of the pion and the nucleon, and  $\epsilon$  represents the energy of the background photon [16]. This process leads to the aforementioned GZK cut-off. The proton is excited to the  $\Delta^+$  resonance by the photon and decays by the strong interaction into a nucleon and a pion in two channels

$$p + \gamma \rightarrow \Delta^+ \rightarrow \begin{cases} n + \pi^+ & \text{with branching ratio } 1/3 \\ p + \pi^0 & \text{with branching ratio } 2/3 \end{cases} . \quad (1.2)$$

Photo-pion production of a nuclei can be approximated by the superposition model, where a nucleus is treated as the superposition of  $Z$  free protons and  $A-Z$  free neutrons. The threshold energy for photo-pion production for heavier nuclei is then proportional to the atomic number as  $E_{thres}^{A,\pi} = E_{thres}^{N,\pi} \cdot A$ .

### 1.3.2 Photodisintegration of Nuclei

Process of photodisintegration happens when a photon is absorbed into a nucleus which leads to an excited state and consequent splitting of the nucleus into two or more parts. Different processes are dominant at different photon energies. At low photon energies, the most relevant process is the giant dipole resonance ("GDR"). The GDR is a collective excitation of the nucleus after an absorption of a photon of energy about 10 to 50 MeV. The GDR usually emits one nucleon, but with lower probability also multiple nucleons or alpha particle can be released as well [17]. At energy about 30 MeV, the quasi-deuteron process becomes comparable to the GDR, and at even higher energies, the total cross section is dominated by this process. The effective energy loss rate can be described as

$$\left. \frac{1}{E} \frac{dE}{dt} \right|_{eff} = \frac{1}{A} \frac{dA}{dt} = \sum_i \frac{i}{A} R_{A,i}(E), \quad (1.3)$$

where  $R_{A,i}$  is the rate for emission of  $i$  nucleons from nucleus with mass number  $A$  [16].

### 1.3.3 Pair Production

Another important process of energy loss of UHECR is electron positron pair production of nucleus  $X$  which can be written as  $\frac{A}{Z}X + \gamma \rightarrow \frac{A}{Z}X + e^+ + e^-$ , where  $A$  is the nucleon number and  $Z$  is the proton number. The threshold energy for pair production is

$$E_{thres}^{\pm} = \frac{m_e(m_X + m_e)}{\epsilon} \approx 4.8 \cdot 10^{17} A \left( \frac{\epsilon}{10^{-3} \text{ eV}} \right)^{-1} \text{ eV}, \quad (1.4)$$

where  $m_e$  and  $m_x$  are the masses of electron/positron and of the nucleus  $X$ , respectively, and  $\epsilon$  represents the energy of the background photon [16].

### 1.3.4 Expansion of the Universe

Cosmic ray particles also lose energy due to the expansion of the Universe. Red-shift energy losses are dominant at low energies, e.i. below the threshold of pair production. Energy losses can be described as

$$-\frac{1}{E} \left( \frac{dE}{dt} \right)_{adiabatic} = H_0, \quad (1.5)$$

where  $H_0$  is the Hubble constant [16].

Energy loss lengths  $\chi_{loss}$  for all the aforementioned processes on CMB and EBL are shown in Figure 1.4 for  $^{14}N$  and in Figure 1.5 for  $^{56}Fe$ . Energy loss length refers to the travelled trajectory over which the particle losses  $1/e$  of its original energy in average. Although  $\chi_{loss}$  for photodisintegration is shown, we need to keep in mind that this process changes the chemical composition of the cosmic-ray particle so the final  $\chi_{loss}$  includes also the energy losses due to the photodisintegration of subsequent lighter nuclei.

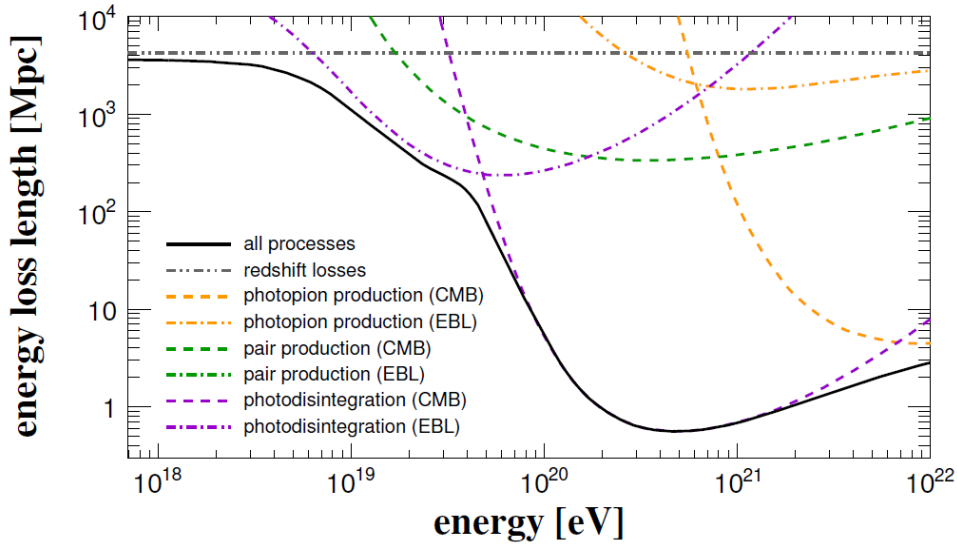
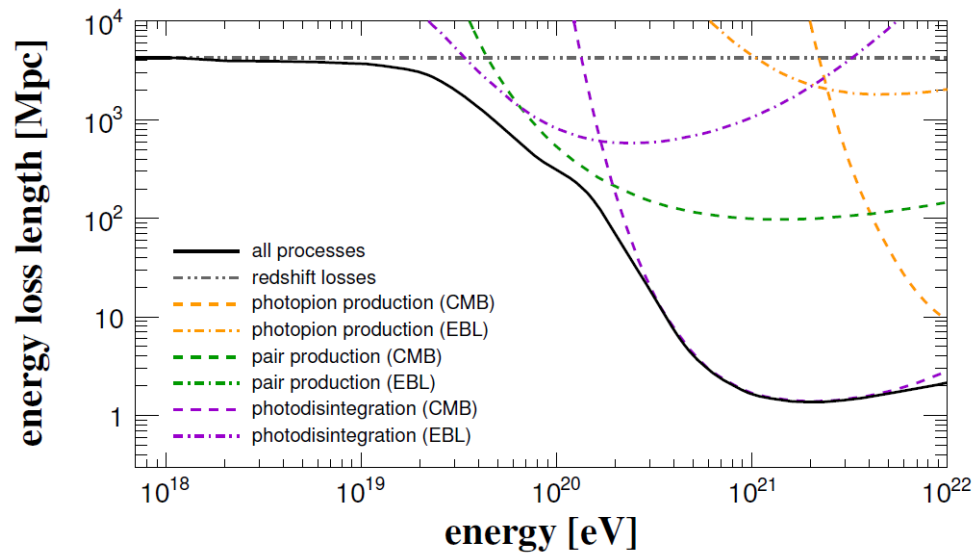


Figure 1.4: Energy loss length for  $^{14}N$  [18].

Figure 1.5: Energy loss length for  $^{56}\text{Fe}$  [18].

# Chapter 2

## The Pierre Auger Observatory

The Pierre Auger Observatory is an experiment dedicated to the study of cosmic rays at the highest energies, that is above  $10^{18}$  eV. The experiment is situated in the Province of Mendoza, Argentina, covering the southern hemisphere of the sky with the mean altitude of detectors of  $\sim 1400$  m. Construction of the observatory began in 2002 and was completed in 2008<sup>1</sup> and so far it is the largest cosmic-ray detector ever built. The aim of the observatory is to reconstruct cosmic-ray showers and determine their energy, mass composition and directions of the primary particles inducing the showers.

### 2.1 Observatory Design

The Pierre Auger Observatory is a hybrid detector with the capability of observing cosmic-ray showers simultaneously by two different techniques - an array of surface detectors ("SD") surrounded by fluorescence detectors ("FD"). While the SD has almost 100% duty cycle and records the particle densities as the shower strikes the ground, the FD measures the longitudinal development of the shower using fluorescence light emitted by nitrogen molecules operating only during dark moonless nights. This hybrid concept is useful for energy calibration of the SD signal by the precise measurement of energy by FD. Besides, it also allows very high accuracy of the determination of the primary particle direction including the time information from SD to FD reconstruction.

There are more than 1660 surface detectors placed in a regular triangular grid. The nearest neighbouring SD station is 1500 m far and the total area of the grid is  $3000 \text{ km}^2$ . There is also a smaller array where the SD stations

---

<sup>1</sup>The construction of the Observatory was completed in 2008 but the Observatory has been collecting data since 2004 [2].

are separated by the distance of 750 m which allows the detection of particles with lower energies, down to  $10^{17}$  eV. The main grid is shown in the Figure 2.1, where each of the dots represents one SD station.

Four air fluorescence detector sites are placed on the border of the array each consisting of six telescopes. The telescopes detect the nitrogen fluorescence light that is emitted during propagation of cosmic-ray shower in the atmosphere. Detection of the fluorescent light was previously used to detect the cosmic-ray showers for example by the by the Fly's Eye experiment [19].

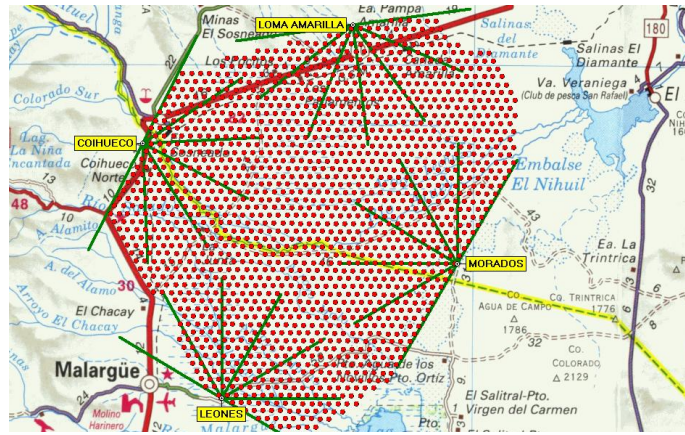


Figure 2.1: The Pierre Auger Observatory. Each dot represents one SD station. Also the four FD sites are shown with indicated field of view of the individual telescopes [2].

### 2.1.1 Surface Detectors

The SD stations are self-powered water-Cherenkov cylindrical tanks each containing 12,000 litres of pure de-ionised water [2] (1.2 m height and diameter of 3.6 m) inside of sealed liner of reflective inner surface. Water Cherenkov detectors were chosen because of their low cost and have many advantages in this type of experiment, such as uniform exposure or sensitivity to not only charged particles but also to high energetic photons. Each station has a GPS receiver which is crucial for event timing and communications synchronization among individual stations. The power for the detector electronics is provided by the solar photovoltaic system.

When an ultra-relativistic charged particle crosses the detector, the Cherenkov light is created in the medium and subsequently collected by three 9-inch photomultiplier tubes that are symmetrically distributed on top of the liner and look downward through windows of clear polyethylene into the wa-

ter. Energy reconstruction from the SD signals is based on the signal density of a given distance from the shower axis. Another important observable derived from SD is the direction of the primary particle which is reconstructed from arrival times of the signals at individual triggered stations.

### 2.1.2 Fluorescence Detectors

There are four sites of air fluorescence detectors (Los Leones, Los Morados, Loma Amarilla, and Coihueco) at the border of the SD array each with six telescopes. The telescopes face inside the array all with the field view of  $30^\circ \times 30^\circ$  covering  $180^\circ$  in azimuth. The telescope has an entrance window, a circular aperture, a corrector ring, a mirror and a camera with photomultipliers. The fluorescence light travels through the UV-passing window and is focused by the mirror into a camera composed of a matrix of 440 pixels located on the focal surface of the telescope [20].

Charged particles created during the development of cosmic ray shower in the atmosphere excite and ionise the nitrogen atoms that afterwards emit the fluorescence light in the wavelength range of  $\sim (300 - 430)$  nm [20]. The fluorescence light is emitted isotropically in the ultraviolet part of the spectrum and is created mainly by the electromagnetic component of the shower. The FD measures the so called longitudinal profile  $\frac{dE}{dX}$ , where  $X$  is the slant depth and  $E$  is the deposited energy. Therefore the  $X_{\max}$  quantity, that is a key observable for the mass composition studies, can be directly measured [2]. Since the produced light is proportional to the collisional energy deposit in the atmosphere, this technique is a near-calorimetric method for determination of the primary energy. Integral of the longitudinal development profile corresponds to approximately 90% of the primary particle's energy [20].

## 2.2 Shower Reconstructions

Recorded signals from surface detectors and fluorescence detectors are inputs to the reconstruction of the air shower geometry, determination of the shower energy and arrival direction or mass composition of the primary particle. Different reconstruction methods are used depending on whether both FD and SD recorded the signal (hybrid reconstruction) or the shower signal was collected only by SD stations.

### 2.2.1 Hybrid Reconstruction

In the hybrid reconstruction, both FD and SD data are used to obtain a final image of the recorded shower.

First step for the reconstruction is the processing of FD signals. The background noise is estimated from the variance of the ADC signals at early time bins, where there is no shower signals. Then all triggered FD pixels are searched for shower signals. Only pulses with signal to noise ratios  $\geq 5$  are taken into account in the reconstruction.

Shower detector plane ("SDP"), which is defined as a plane containing shower axis and triggered fluorescence telescopes, is obtained from the telescope data by minimalization of the function

$$S = \frac{1}{\sum_i q_i} \sum_i q_i \left( \frac{\frac{\pi}{2} - \arccos(\vec{p}_i \cdot \vec{n}_\perp^{SPD})}{\sigma_{SPD}} \right)^2 \quad (2.1)$$

over all pulses  $i$ , where  $q_i$  is the integrated signal in pixels,  $\vec{n}_\perp^{SPD}$  is a vector normal to the SDP in spherical coordinates,  $\vec{p}_i$  is the pointing direction of the pixel and  $\sigma_{SPD}$  is the pointing uncertainty for the SDP fit, which was evaluated as  $0.35^\circ$  [2].

Time information ( $t$ ) of each triggered FD pixel is used to fit three important parameters  $T_0$ ,  $R_p$  and  $\chi_0$  depicted in Figure 2.2 that describes the angular movement of the shower within the SDP seen by the triggered telescope

$$t(\chi_i) = T_0 + \frac{R_p}{c} \tan \left( \frac{\chi_0 - \chi_i}{2} \right), \quad (2.2)$$

where  $c$  is the speed of light and  $\chi_i$  is the angle of  $i$ th pixel along the SDP with respect to the horizontal axis at the telescope.  $T_0$  stands for the time of the closest approach of the shower to the fluorescence detector,  $R_p$  corresponds to the perpendicular distance between the telescope and the shower axis and  $\chi_0$  is the angular orientation of the shower axis.

Light collected by FD as a function of time is converted to the energy deposited by the shower as a function of the slant depth  $X$ . The longitudinal profile of energy deposit is obtained from the fit by the so called Gaisser-Hillas function [21]

$$f_{GH}(X) = \left( \frac{dE}{dX} \right)_{max} \left( \frac{X - X_0}{X_{max} - X_0} \right)^{(X_{max} - X_0)/\lambda} \cdot e^{(X_{max} - X)/\lambda}, \quad (2.3)$$

where  $\left( \frac{dE}{dX} \right)_{max}$  is the maximum of the energy deposit at depth  $X = X_{max}$  and  $X_0$  and  $\lambda$  are fitted parameters. The  $X_{max}$  quantity is then derived as one

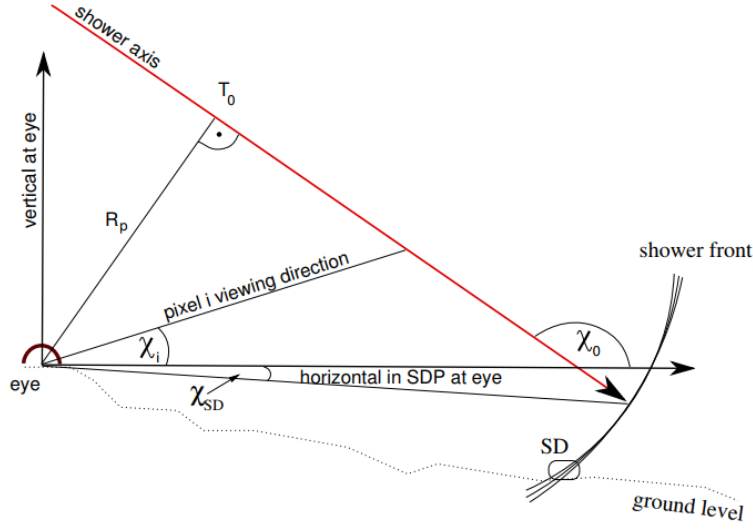


Figure 2.2: Hybrid reconstruction of the air shower [2].

of the fitted parameters. Shower reconstruction by fluorescence detectors is significantly improved by including the timing information from the triggered surface detectors.

### 2.2.2 SD Reconstruction

An air shower initiated by high energetic cosmic-ray particle, above  $10^{19}$  eV, extends over more than  $25 \text{ km}^2$  on the ground inducing signals in multiple surface detector stations. Timing and sizes of signals in individual stations are vital parameters for the reconstruction of the shower energy and arrival direction of the primary particle.

Shower geometry is obtained by fitting the start times of the signal in each individual station  $t_i$  to the plane front. The shower front development is approximated with a speed-of-light inflating sphere.

The lateral distribution function ("LDF") of the SD signals is described by a modified Nishimura-Kamata-Greisen function [22, 23]

$$S(r) = S(r_{opt}) \left( \frac{r}{r_{opt}} \right)^\beta \left( \frac{r + r_1}{r_{opt} + r_1} \right)^{\beta + \gamma}, \quad (2.4)$$

where  $S$  is the predicted signal at distance  $r$  from the shower axis,  $r_{opt}$  is the optimum distance selected as 1000 m,  $r_1$  was chosen to 700 m and  $\beta$  and  $\gamma$  are fitted parameters. An example of dependence of the signal size on the

distance from the shower core is shown in Figure 2.3. Axis of the shower  $\hat{a}$  is obtained from the shower impact point on the ground  $x_{gr}^{\rightarrow}$  and from the virtual shower origin  $x_{sh}^{\rightarrow}$  from the geometrical reconstruction as

$$\hat{a} = \frac{x_{sh}^{\rightarrow} - x_{gr}^{\rightarrow}}{|x_{sh}^{\rightarrow} - x_{gr}^{\rightarrow}|}. \quad (2.5)$$

The angular resolution for events with more than three activated stations is better than  $1.6^\circ$  and for events with more than six activated stations it is better than  $0.9^\circ$  [2] for events with an energy above  $3 \cdot 10^{18}$  eV.

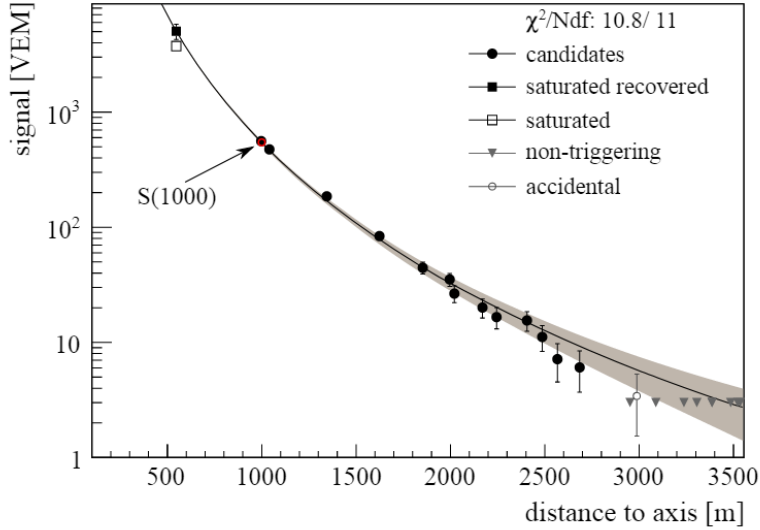


Figure 2.3: Dependence of the signal size on the distance from the shower core for a typical event detected in SD of the Pierre Auger Observatory [2].

The value of  $S(1000)$  decreases with zenith angle  $\theta$  for a given energy. The shape of the attenuation curve  $f_{CIC}(\theta)$  was extracted from the data by the Constant Intensity Cut method [24]. The median angle  $\bar{\theta} = 38^\circ$  is used to define  $S_{38} = S(1000)/f_{CIC}(\theta)$ , which corresponds to the signal produced by a shower with size  $S(1000)$  arriving from  $\theta = 38^\circ$ .  $S_{38}$  is than directly related to the shower energy.

### 2.2.3 Shower Universality Reconstruction

Shower maximum  $X_{max}$  is one of the most sensitive quantities to the mass composition of the primary particles. It can be reconstructed from the signals of fluorescence detectors. Such reconstruction has a strong disadvantage that

it can not be applied at any time, but only when there is a minimal background light. This was a motivation for the invention of a new procedure to reconstruct the shower maximum using only the information from surface detectors. It is of high importance because it can increase the statistics for mass composition studies at the highest energies. Such procedure was recently presented in [25, 26]. This so called shower universality reconstruction introduces four components of the detected shower

1. the muonic component,
2. the electromagnetic component originating from muon interactions and muon decay,
3. the purely electromagnetic component and
4. the jet component, that is the electromagnetic component coming from low-energy hadrons [26].

A shower is characterized by its energy  $E$ , shower maximum  $X_{\max}$ , zenith angle  $\theta$ , air density on the ground  $\rho_{\text{ground}}^{\text{air}}$  and number of muons on the ground  $N_{\mu}$ . Signal induced in surface detector in a distance  $r$  and orientation of shower direction with azimuthal angle  $\Psi$  from the shower axis is then parametrized as

$$\begin{aligned}
 S(r, \Psi | E, X_{\max}, N_{\mu}, \theta, \rho_{\text{ground}}^{\text{air}}) = & \\
 & \sum_{i=1, \dots, 4} S_0^i(r, \Delta X | E) \cdot f_{\text{mod}}^i(r, \Psi | \theta) \\
 & \cdot f_{\text{atm}}^i(r | \rho_{\text{ground}}^{\text{air}}) \cdot f_{\text{conv}}^i(r, \Delta X, \Psi | \theta) \\
 & \cdot f_{N_{\mu} \text{fluc}}^i(r | N_{\mu}), \tag{2.6}
 \end{aligned}$$

where the distance of the shower maximum to the ground  $\Delta X$  depends on the set of parameters  $(r, \Psi, \theta, X_{\max})$  and  $i$  refers to the four electromagnetic components of the shower [26]. Terms in the sum correspond to the signal induced in an ideal detector, correction for atmospheric effects, conversion factor for realistic detector and a factor correlating fluctuations in the muon number  $N_{\mu}$ , respectively. Accuracies of  $X_{\max}$  reconstruction for the Pierre Auger Observatory surface detectors are calculated to  $\approx 45 \text{ g/cm}^2$  at  $10^{19} \text{ eV}$  [25].

## Chapter 3

# Simulation of Propagation of Cosmic-ray

The UHECR is usually thought to be of an extragalactic origin. This hypothesis is supported by the fact that the galactic plane does not correlate with arrival directions of the particles with energies above  $\sim 10^{18}$  eV as the arrival directions are rather isotropic. Since the high-energetic particles most likely travel a long distance from the source to the Earth (in orders even tens of megaparsecs) the original particles from the source might differ very much from the ones we observe at the Earth because of the processes described in Section 1.3. For this purpose, simulation frameworks are being developed for the propagation of UHECR. One of them is CRPropa that was used for purposes of this research work and it will be briefly described in the following. The other public code used by the cosmic-ray community, SimProp, is described here as well.

### 3.1 CRPropa

CRPropa is a publicly available code to simulate the propagation of UHECR in the Universe. We used the newest version of the code CRPropa 3 [27]. The interactions of the particles with ambient photons (CMB and infra-red background ("IRB")) that are included in CRPropa are the photo-pion production, electron-pair production, photodisintegration of the nucleus, nuclear decay and red-shift. The spectral shape of the CMB is well known but IRB is not that well measured and it is described by various models that are optional in the code. In this work, the default model of IRB Dominguez 2011 [28] was used. The electron pair production is approximated as continuous energy loss given by its low energy threshold. Simulations can be run in

one-dimensional or three-dimensional space.

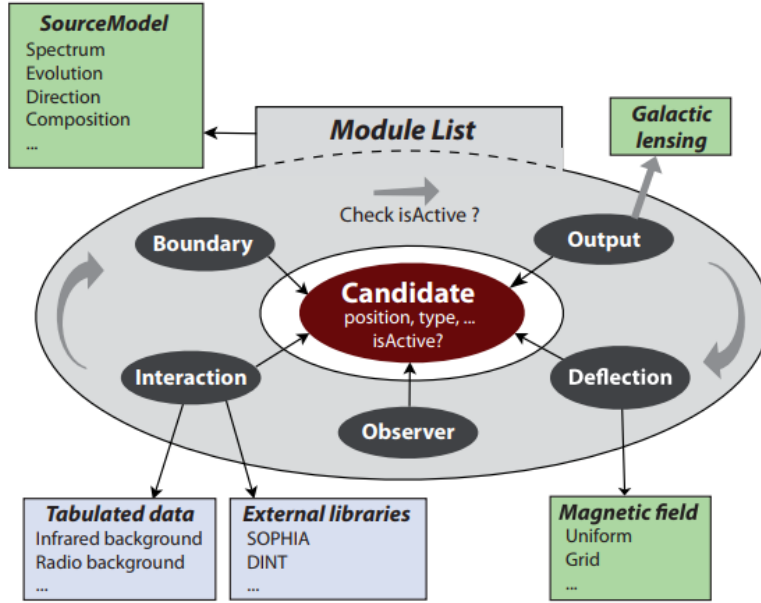


Figure 3.1: Illustration of the CRPropa 3 modular structure [27].

The code simulates movement of injected particles in the given space with source distribution and magnetic fields. In the one-dimensional simulations, the deflections by magnetic field are not taken into account, only the aforementioned interactions with ambient photons cause energy losses and/or a change of particle type. The output of the simulation is a set of position, energy and particle ID for each step of the simulation and each individual injected particle and its secondaries. In the three-dimensional simulation, the path and properties of the injected particle and its secondaries are calculated from Lorentz equations and interactions with ambient photons. The output in this case is a set of position and momentum components, energy, travelled distance and particle ID for particles reaching the observer [29]. Since the distances between the sources and observer are in orders of Mpc, the observer is usually simulated as an observer sphere of quite large radius so that sufficient amount of particles reach the observer. Another approach used in the galactic propagation simulations is the backtracking of cosmic rays with opposite charge from the observer to the edge of the Galaxy, which reduces the computational time since all the particles are included in the final output. However, backtracking can be used in extragalactic propagation of UHECR only for protons given the fact it can not simulate (back)photodisintegration

of nuclei and other energy losses, therefore its use is mainly in arrival direction studies.

The CRPropa 3 is written in C++ and interfaced into Python. SWIG allows to work with both Python scripts and custom or existing C++ modules [27]. The simulation is divided into modules where the separate properties of the simulation are set, such as properties of the source, properties of the observer, included particle interactions etc. The modules are mutually independent. The modular structure is visualised in Figure 3.1.

CRPropa 3 can simulate any custom magnetic field including galactic and extragalactic magnetic fields. Some models of galactic magnetic fields are implemented into the simulation code and can be easily used by the user including Jansson & Farrar model [30] and Pshirkov et al. model [31].

## 3.2 SimProp

Another simulation code for the UHECR propagation is SimProp [32]. SimProp is a one-dimensional algorithm where magnetic fields are not included into computations and only interactions with CMB and EBL are influencing the propagated particle state.

Protons simulated with SimProp interact only with CMB in the form of electron pair production and photo-pion production. The interaction with EBL is neglected. Heavier nuclei interact on CMB by electron pair production and on both CMB and EBL by photodisintegration of nucleus. Photo-pion production is neglected for heavier nuclei. The code can simulate propagation of nuclei of atomic number  $A = 2$  up to  $A = 56$  with one stable isotope for each atomic mass. The computations of particle properties during propagation are based on the continuous energy loss approximation and an exact conservation of the particle's Lorentz factor in the photo-disintegration process. The code also includes the adiabatic energy loss over time due to the expansion of the Universe given by equation (1.5) or in the case of change of the Lorentz factor  $\Gamma$

$$-\frac{1}{\Gamma} \left( \frac{d\Gamma}{dt} \right)_{adiabatic} = H(z), \quad (3.1)$$

where  $H(z) = H_0 \sqrt{(1+z)^3 \Omega_m + \Omega_\lambda}$  is the Hubble parameter at red-shift  $z$ ,  $H_0 = 71$  km/s/Mpc is the Hubble constant,  $\Omega_m = 0.24$  is the density of matter and  $\Omega_\lambda = 0.72$  correspond to the density of dark energy. These values are taken from WMAP data [33].

The code is developed in C++. Initial parameters of the Monte Carlo simulations are red-shift of the source, type of the primary nucleus and in-

jection energy at the source. The code computes the propagation in steps of red-shift in one dimension up to the observer at red-shift equal to zero. Sim-Prop follows propagation of the original nuclei and its secondary nuclei and protons created by photodisintegration. Nuclei are following a branch of the code where all of the interactions happen and the energy and/or the type of nucleus changes. This process continues in steps up to  $z = 0$ . The intervals in red-shift have an exponentially decreasing size towards the source, or to the original point of the nucleus creation.

The output is in the form of ROOT file containing information about the propagation in individual branches with information about branch, energy of the particle, the mass and the charge of the nucleus, the initial and final energy and red-shift, the number of the interactions suffered by the current particle and the distance covered in the current step [32].

# Chapter 4

## Results

The first part of this section is dedicated to the obtained results regarding application of the universality reconstruction on the Pierre Auger Observatory data. In the second part, results from simulations of the propagation of cosmic-ray particles through the Universe made with CRPropa 3 framework [27] will be discussed.

### 4.1 Shower Maximum measured by the Pierre Auger Observatory

We applied the parametrization of universality reconstruction described in Section 2.2.3 to the Pierre Auger Observatory ADST [34] data for events measured by surface detectors. Firstly, we used the common cuts for the SD data of period from 25/8/2004 to 17/11/2016, namely *SD1500 vertical cuts*, which selected total of 92298 events with energy  $E \geq 3.162 \cdot 10^{18}$  eV. *SD1500 vertical cuts* rejects lightnings and require the shower to be fully reconstructed, the energy to be  $\log(E/\text{eV}) > 17.5$ , zenith angle  $\theta \leq 60^\circ$  and T4 and T5 trigger equal to 2 (see [2]). Events detected during so called bad periods are excluded as well. Following cuts on reconstructed quantities had to be applied according to [35] to get reliable results of reconstructed shower maximum by the universality reconstruction:

- The reconstructed shower maximum must be in the interval  $X_{\text{max}} \in (500, 1150) \text{ g} \cdot \text{cm}^{-2}$ .
- $R_\mu$ , which represents the relative rescaling of the muon number, must be  $R_\mu \in (0.5, 3)$ .

- Difference between the reconstructed zenith angle from universality  $\theta_{uni}$  and from the classic SD reconstruction  $\theta_{SD}$  have to fulfil  $|\theta_{uni} - \theta_{SD}| \leq 5^\circ$ .
- Reconstructed SD energy must be  $E \geq 10^{19}$  eV.
- Reconstructed SD zenith angle must be lower than  $54^\circ$ .

After applying these cuts, the total number of events selected for the mass composition analysis decreased to 6693.

Obtained dependency of the mean value of the shower maximum on energy of the primary particle is shown in Figure 4.1, where it is also compared with predictions of hadronic interaction models EPOS-LHC and QGSJet II-04. The predictions for the two models of hadronic interactions were taken from [36]. The same dependency is shown in Figure 4.2 for different energy binning corresponding to energy bins chosen by Pierre Auger Collaboration for  $X_{max}$  analysis obtained from FD. Official values of mean  $X_{max}$  taken from [37], used in [15], are also shown in Figure 4.2. We can see that the universality reconstruction can not cover as wide energy range as the FD reconstruction when we compare it with Figure 1.2, but the trend at the highest energies is the same, the mass composition of cosmic rays tends towards heavier primary particles. Significance of the last two bins in Figure 4.1 is questionable since the statistics for these highest energies is very low. The resolution by FD in this energy range is decreasing from 20 g/cm<sup>2</sup> to 14 g/cm<sup>2</sup> [38] while the accuracies of  $X_{max}$  universality reconstruction for the Pierre Auger Observatory surface detectors are calculated to  $\approx 45$  g/cm<sup>2</sup> at  $10^{19}$  eV [25].

The distribution of  $X_{max}$  in individual bins corresponding to the same binning as in Figure 4.2 is shown in Figure 4.3, where the distribution is fitted by generalized Gumbel distribution function [39] in the form of

$$\mathcal{G}(z) = \frac{1}{\sigma} \frac{\lambda^\lambda}{\Gamma(\lambda)} e^{-\lambda z - \lambda e^{-z}}, \quad z = \frac{x - \mu}{\sigma}, \quad (4.1)$$

where  $\mu$  and  $\sigma$  are location and scale parameters, related to the mean and the spread of the distribution and  $\lambda$  is the shape parameter. Mean value  $\mu$  and variance  $\sigma^2$  of the distribution are given by

$$\mu = \sigma[\psi(\lambda) - \ln(\lambda)], \quad \sigma^2 = \frac{1}{\psi'(\lambda)}, \quad (4.2)$$

where  $\psi(\lambda)$  is the digamma function defined as

$$\psi(\lambda) = \frac{d}{d\lambda} \ln \Gamma(\lambda) = \frac{\Gamma'(\lambda)}{\Gamma(\lambda)}. \quad (4.3)$$

The equation (4.1) describes a spread of the extremal values of a stochastic variable and while it is not the exact distribution expressing the  $X_{\max}$  distribution it describes the data relatively well.

Fractions of p, He, N and Fe on the Earth obtained from the Pierre Auger Observatory data were studied in [15]. In their research they used different models of hadronic interactions to get the mass decomposition. The resulting primary fractions are demonstrated in Figure 4.4.

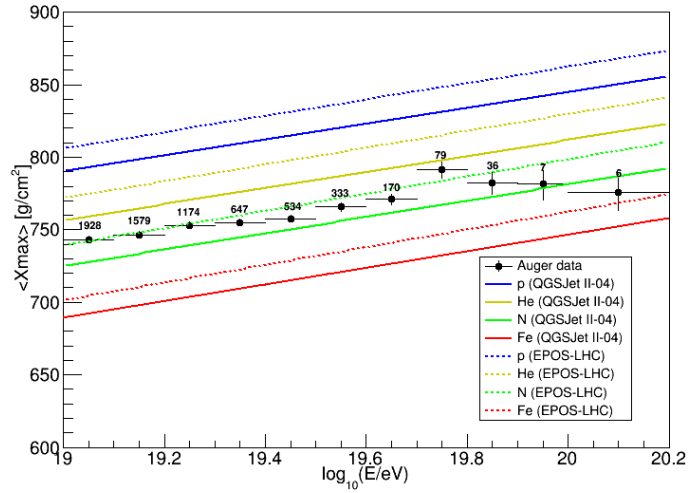


Figure 4.1: Mean value of shower maximum obtained from universality reconstruction depending on energy of the primary particle compared with model prediction for EPOS-LHC and QGSJetII-04. For each bin number of events is listed.

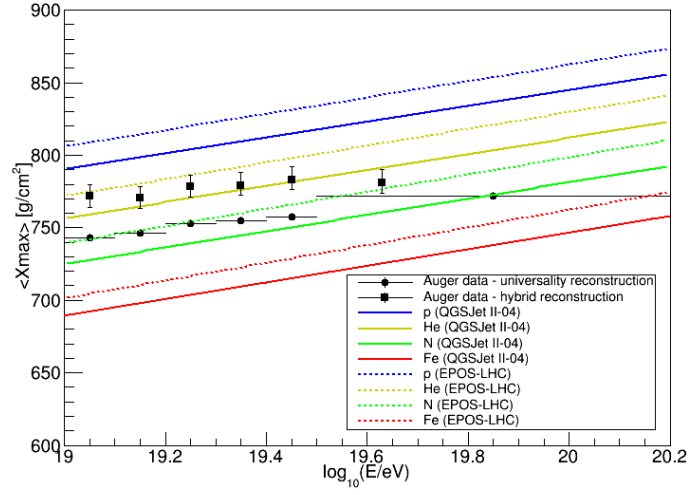


Figure 4.2: Mean value of shower maximum obtained from universality reconstruction and FD reconstruction [37] depending on energy of the primary particle compared with model prediction for EPOS-LHC and QGSJetII-04.

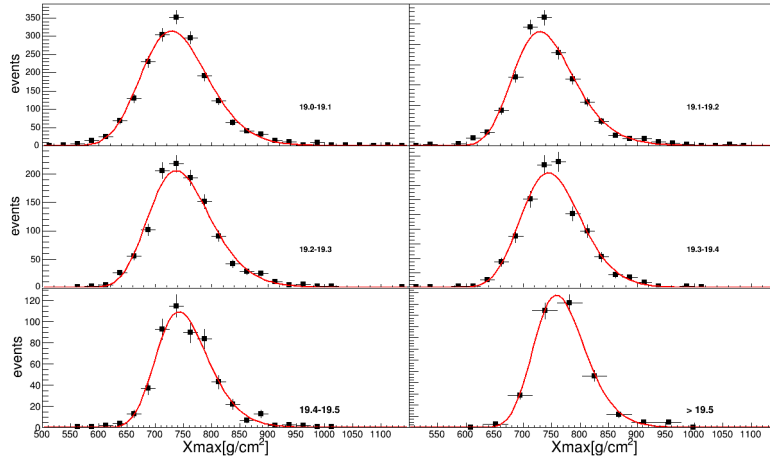


Figure 4.3: Distribution of  $X_{\max}$  reconstructed from SD data in individual energy bins fitted with generalized Gumbel distribution function (4.1).

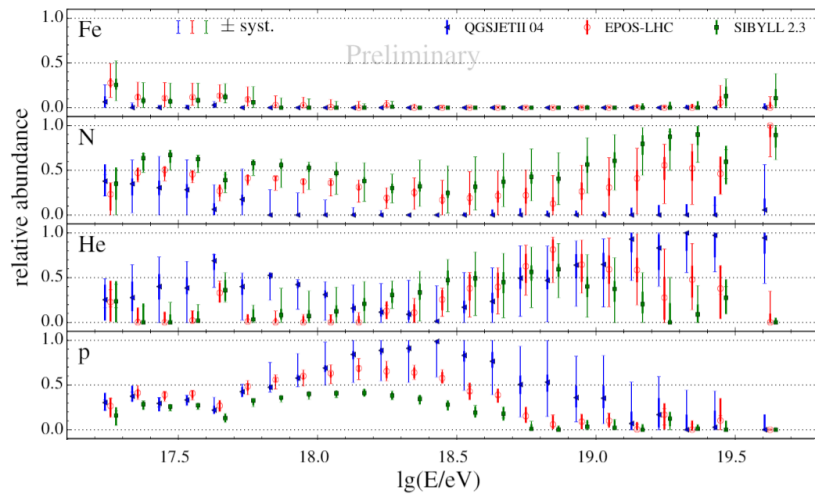


Figure 4.4: Fitted fractions of individual elements using different models in case of mixed composition from the Pierre Auger data. Modified plot from [15].

## 4.2 Simulated Propagation of Cosmic Rays

This section is dedicated to the results of simulations of propagation of cosmic-ray particles in the Universe obtained with program CRPropa3 described in section 3.1. So far, the simulations were made as 1D simulations, where deflections by galactic and extragalactic magnetic fields are not included.

### 4.2.1 Propagation of Cosmic Rays in the Universe

First topic that was studied is the significance of different types of energy losses on the propagation of the primary particle. Energy loss lengths depending on their primary energy for photo-pion production and electron pair production on CMB together with adiabatic losses due to expansion of the Universe are shown in Figures 4.5, 4.6, 4.7 and 4.8 for four types of primary particles: protons, helium nuclei, nitrogen nuclei and iron nuclei, respectively. Photodisintegration of the nuclei is not included in the plots because the final energy loss length would not be related to only one type of nucleus. At the lowest energies, the red-shift is the leading energy loss, while at higher energies, other processes become dominant. We can also see that energy loss lengths for photo-pion production and electron pair production are dependent on the atomic number of the particle as can be also seen from equations (1.1) and (1.4).

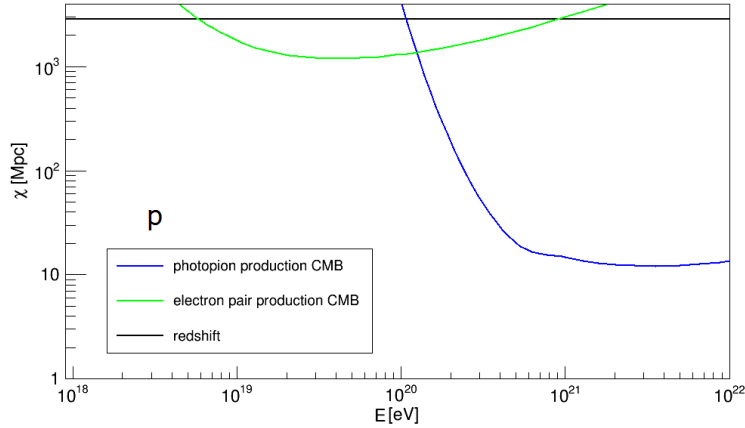


Figure 4.5: Energy loss length  $\chi$  for photo-pion production, electron pair production and red-shift for protons on CMB depending on the energy of proton computed from simulations in CRPropa3.

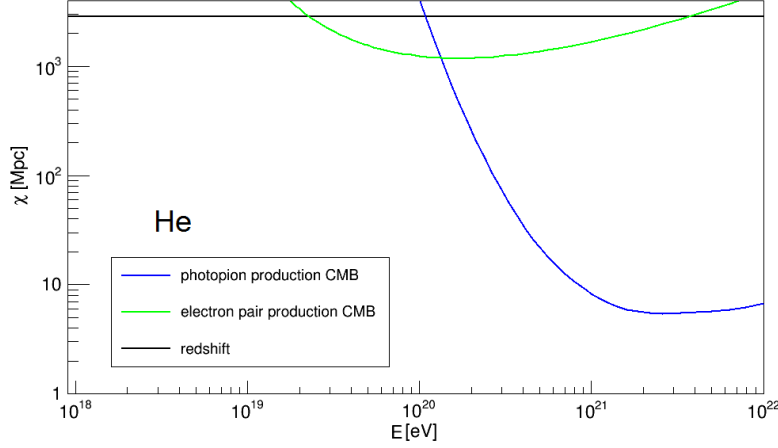


Figure 4.6: Energy loss length  $\chi$  for photo-pion production, electron pair production and red-shift for helium nuclei on CMB depending on the energy of He computed from simulations in CRPropa3.

As the particle travels from its source to the Earth it loses energy. The effect of the total energy losses is illustrated in Figures 4.9, 4.10, 4.11 and 4.12 for four types of primary particles, respectively. Four primary energies  $10^{19}$  eV,  $10^{20}$  eV,  $10^{21}$  eV and  $10^{22}$  eV are shown. Every simulation included one source in the distance of 1100 Mpc, that emitted 10 000 primaries with one of the mentioned energies and the step in distance was chosen to be 1 Mpc. For illustration, a line is drawn referring to the energy  $10^{20}$  eV, which is almost the highest energy observed in cosmic rays on the Earth<sup>1</sup>. We can see that the energy rapidly decreases with travelled distance and the rate of energy losses increases with the energy. While the energy losses over the travelled distance are very similar for the case of primary protons and primary helium nuclei (illustrated in Figure 4.9 and 4.10, respectively), the energy losses over distance for nitrogen and iron nuclei (Figure 4.11 and 4.12, respectively) show slightly different behaviour. Such effect is caused by the photodisintegration of nuclei. We can see, that even after only 1 Mpc the primary energy of  $10^{22}$  eV already decreased under  $10^{21}$  eV for both primary nuclei because of the high photodisintegration cross section. The evolution of the energy from the source to 10 Mpc for nitrogen as primaries is demonstrated in Figure 4.13, where we can observe a steep fall of the

<sup>1</sup>The cosmic-ray particle with the highest energy observed so far was the so-called "Oh-My-God particle" with estimated energy of  $(3.0 \pm_{-0.54}^{+0.36}) \cdot 10^{20}$  eV detected in 1991 by the Fly's Eye Cosmic Ray Detector [40].

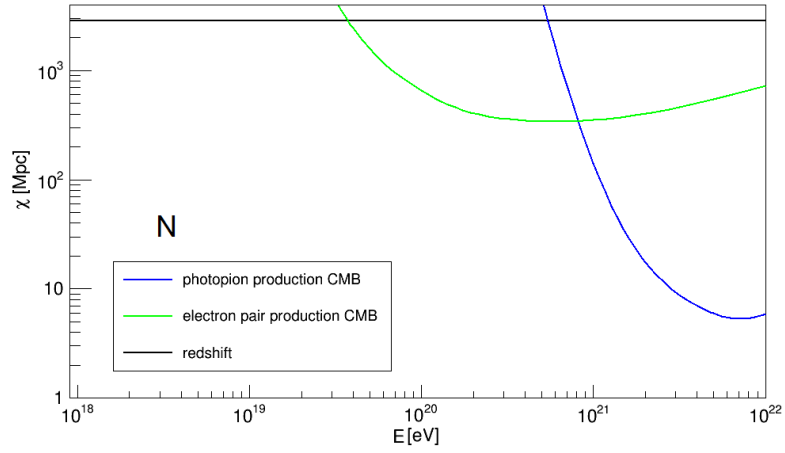


Figure 4.7: Energy loss length  $\chi$  for photo-pion production, electron pair production and red-shift for nitrogen nuclei on CMB depending on the energy of N computed from simulations in CRPropa3.

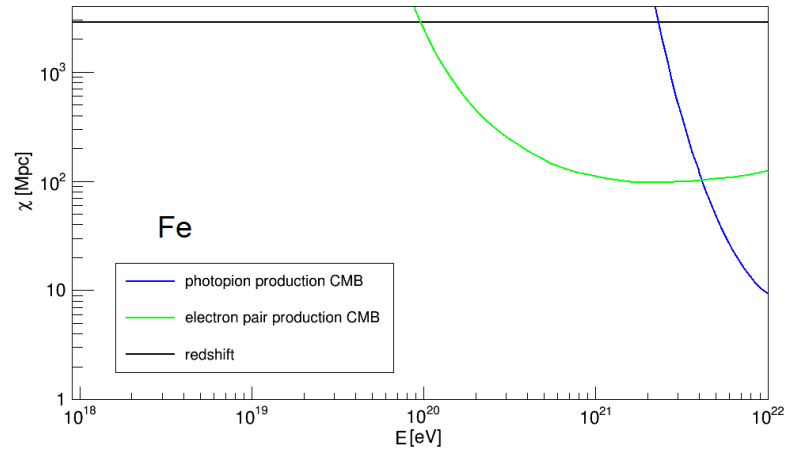


Figure 4.8: Energy loss length  $\chi$  for photo-pion production, electron pair production and red-shift for iron nuclei on CMB depending on the energy of Fe computed from simulations in CRPropa3.

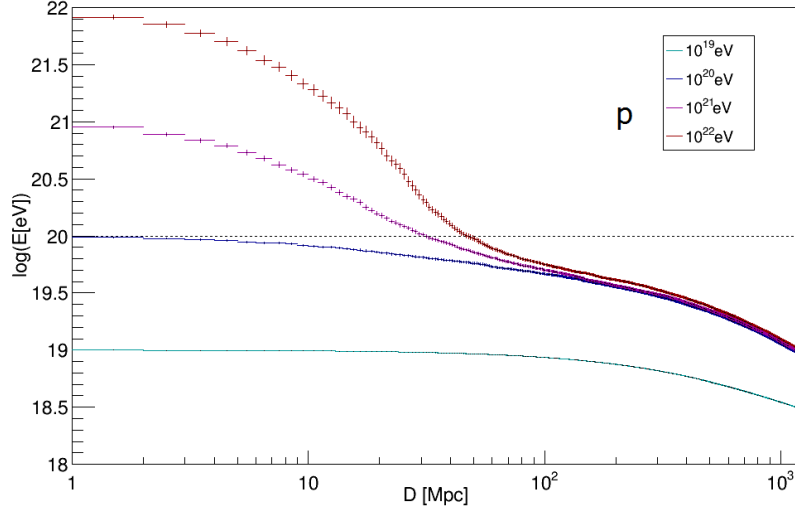


Figure 4.9: Mean energy of the particles over distance travelled from the source to the observer at 1100 Mpc for primary protons of four different primary energies.

energy between the source and the distance of 1 Mpc. If we suppose that the sources of the UHECR do not emit particles with energies higher than  $10^{22}$  eV, the sources of the most energetic events (about  $10^{20}$  eV) should be closer than  $\sim 50$  Mpc and even closer for sources emitting heavier primaries. In the case of source emitting iron nuclei, we would be able to observe a particle with energy higher than  $10^{20}$  eV only if the source was closer than 20 Mpc. Higher primary energies should not change this statement, since the energy losses would only rapidly increased than for the maximal energy  $10^{22}$  eV that was simulated in this study. However, these implications are made based on the knowledge of energy losses and CMB density that could be different in reality.

Not only the energy of the primary particle is changed during its propagation, but also the type of the particle can be modified as heavier nuclei can disintegrate on CMB. This phenomena will be investigated in more detail in the following section, but for better understanding of the process the development of the mean atomic number along the particle trajectory is illustrated in Figure 4.14. Here we can clearly see how the atomic number decreases with the travelled distance. The data are from a simulation with one source in distance 1100 Mpc emitting 1000 nitrogen nuclei with the energy  $10^{19}$  eV.

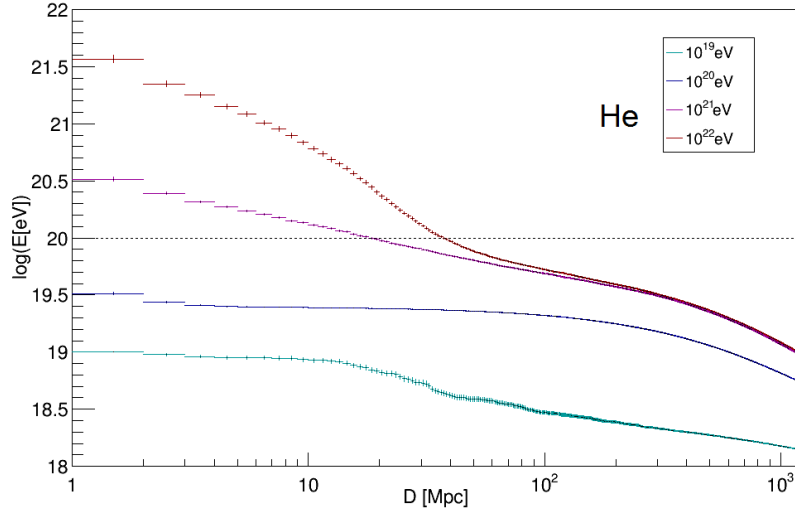


Figure 4.10: Mean energy of the particles over distance travelled from the source to the observer at 1100 Mpc for primary helium nuclei of four different primary energies.

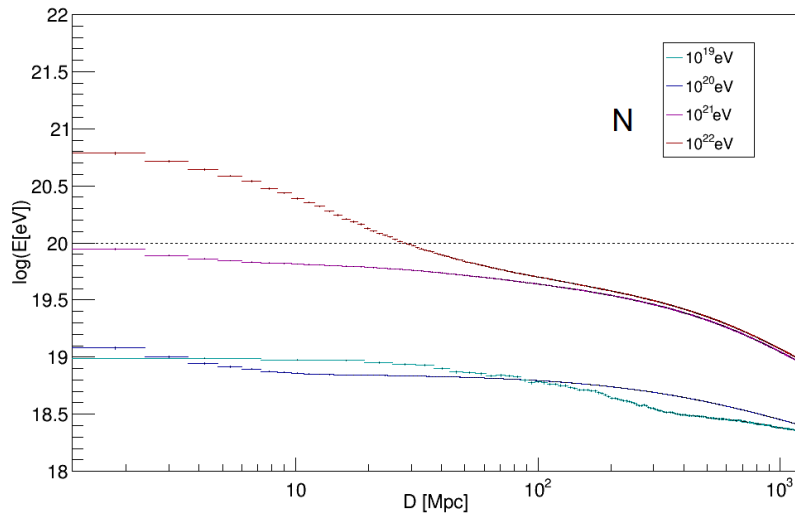


Figure 4.11: Mean energy of the particles over distance travelled from the source to the observer at 1100 Mpc for primary nitrogen nuclei of four different primary energies.

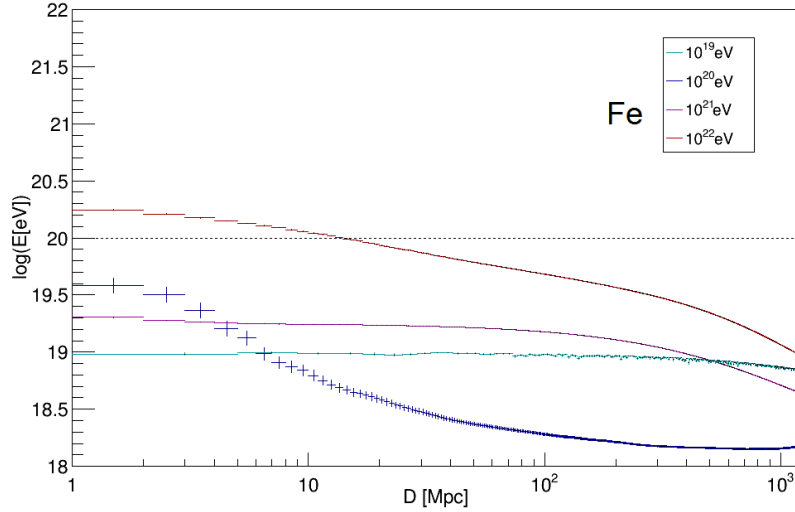


Figure 4.12: Mean energy of the particles over distance travelled from the source to the observer at 1100 Mpc for primary iron nuclei of four different primary energies.

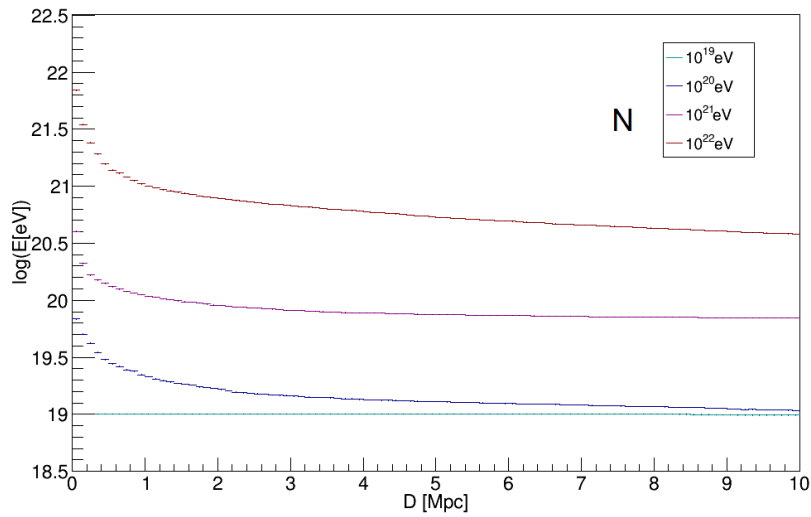


Figure 4.13: Mean energy of the particles over distance travelled from the source to the distance of 10 Mpc for primary nitrogen nuclei of four different primary energies.

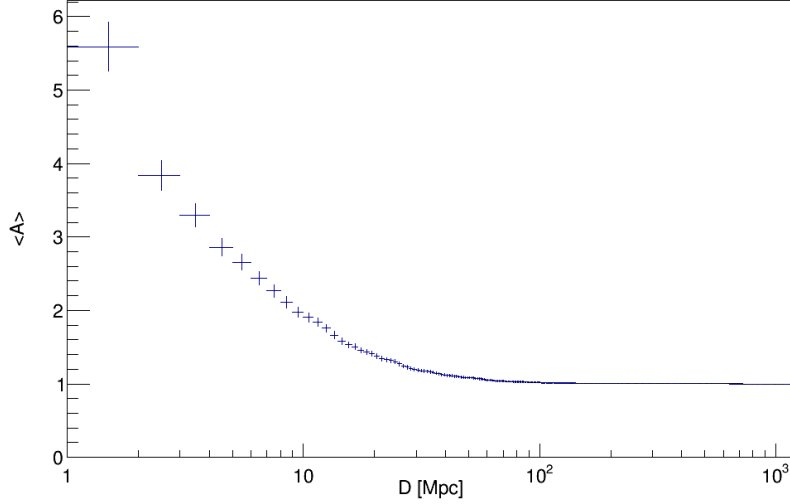


Figure 4.14: Evolution of the mean nucleon number  $A$  during propagation in the Universe over the distance  $D$  for a primary nitrogen nuclei.

## 4.2.2 Observation at the Earth

This section is dedicated to the final form of simulated cosmic rays from the source as it would be seen for an observer on the Earth. All simulations are again only in 1D therefore deflections in magnetic fields are not taken into account.

We focused on two main phenomena. The first one is the fraction of observed helium nuclei on the Earth, which was investigated for a source of mixed composition (25% protons, 25% helium nuclei, 25% nitrogen nuclei and 25% iron nuclei) and the power law energy spectrum with spectral index of 2 covering the range from the minimal energy  $E_{\min}^{\text{Source}} = 3 \text{ EeV}$  to the maximal rigidity  $R_{\max}^{\text{Source}} = 100 \text{ EeV}$ . Simulations were made separately for the individual elements, each with 1000 primary particles for a source in a given distance. Distance of the source was chosen as 1 Mpc, and from 2.5 Mpc to 30 Mpc with step of 2.5 Mpc. Three energy intervals of the final cosmic rays hitting Earth were studied  $\log(E^{\text{Earth}}/\text{eV}) = (18.5 - 19.0)$ ,  $\log(E^{\text{Earth}}/\text{eV}) = (19.0 - 19.5)$  and  $\log(E^{\text{Earth}}/\text{eV}) > 19.5$ . The resulting dependencies of the He fraction arriving on the Earth on the source distance are shown in Figures 4.15, 4.16 and 4.17 for energy at Earth  $\log(E^{\text{Earth}}/\text{eV}) = (18.5 - 19.0)$ ,  $\log(E^{\text{Earth}}/\text{eV}) = (19.0 - 19.5)$  and  $\log(E^{\text{Earth}}/\text{eV}) > 19.5$ , respectively.

We can see that with such initial conditions (power law spectrum and

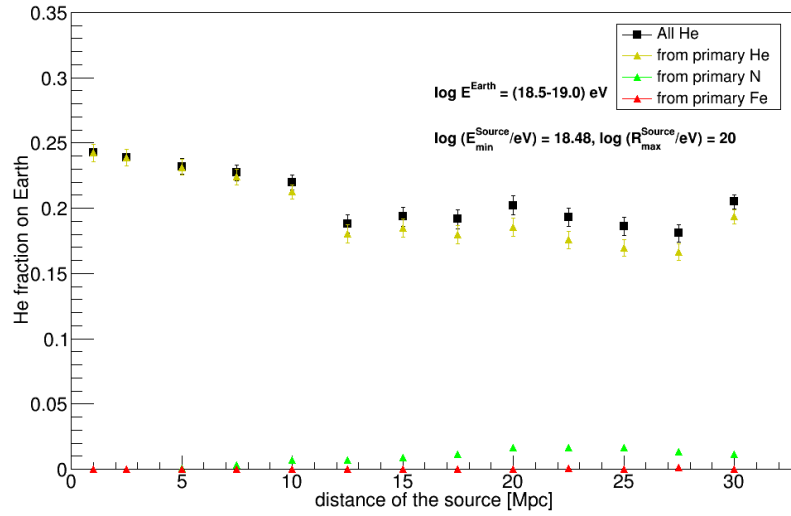


Figure 4.15: Fraction of helium nuclei hitting Earth with energy in the range  $\log(E^{\text{Earth}}/\text{eV}) = (18.5 - 19.0)$  for different distances of the source. The source composes of 25% p, 25% He, 25% N and 25% Fe.

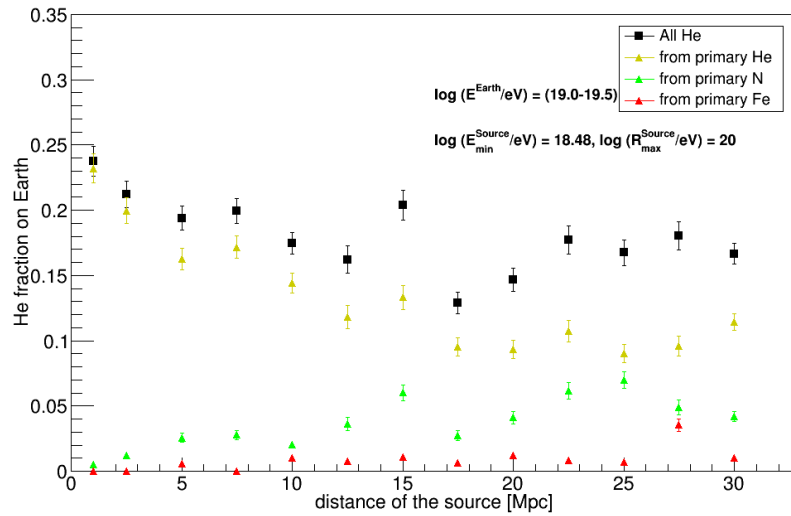


Figure 4.16: Fraction of helium nuclei hitting Earth with energy in the range  $\log(E^{\text{Earth}}/\text{eV}) = (19.0 - 19.5)$  for different distances of the source. The source composes of 25% p, 25% He, 25% N and 25% Fe.

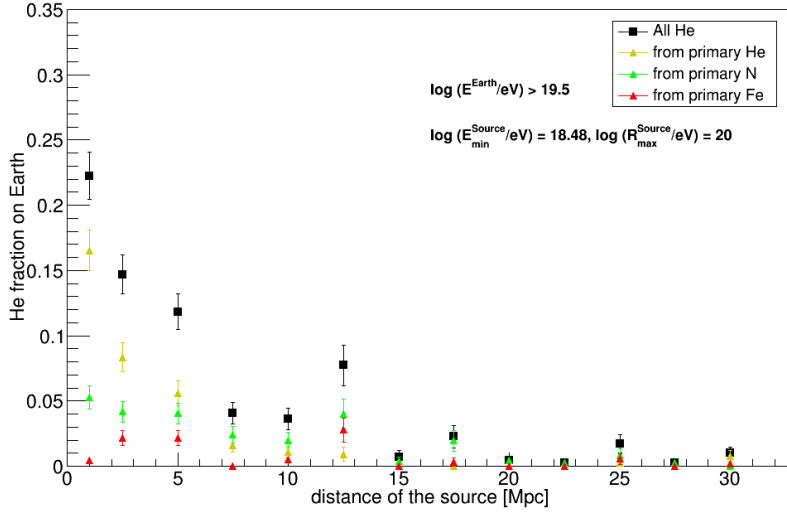


Figure 4.17: Fraction of helium nuclei hitting Earth with energy  $\log(E^{\text{Earth}}/\text{eV}) > 19.5$  for different distances of the source. The source composes of 25% p, 25% He, 25% N and 25% Fe.

composition of the source) the fraction of observed helium nuclei on Earth is under 25% for all three chosen energy ranges and all source distances. In the case of  $\log(E^{\text{Earth}}/\text{eV}) = (18.5 - 19.0)$  and  $\log(E^{\text{Earth}}/\text{eV}) = (19.0 - 19.5)$  most of the helium nuclei hitting Earth actually come from the primary He from the source and primary N and Fe do not contribute as much, especially for the lowest energy range, where the fraction of He on Earth originating from primary N is under 2% for all source distances and a completely negligible percentage comes from the primary Fe.

It is interesting that for the lowest energy range (see Figure 4.15), the fraction of He on Earth is almost the same (from 17% to 25%) with a small decrease with distance. The cross section for He disintegration is very low on these energies of the source so almost all the energy losses are due to photo-pion production, electron pair production and red-shift. The small steady decrease with distance ( $\sim 3\%$  per 10 Mpc) is caused by the longer trajectory along which the original nucleus can loose energy. The additional small deviations of the steady trend of the He fraction are on the one hand caused by contributions of other primaries and on the other hand due to the small, but non-zero, probability of He disintegration.

Official results of fitted fractions of He from Figure 4.4 shown in Section 4.1 indicate a high He fraction for energies above  $\log(E^{\text{Earth}}/\text{eV}) = 18.5$  in

comparison with our studied simulations, although the uncertainties are too high to make final assumptions. If the real He fraction would actually be much higher than 20%, than it might probably come from a source emitting mainly helium nuclei. Generally, to exactly predict the characteristics of such sources would still be very difficult since the space of free parameters is quite large.

Second phenomenon which will be depicted in this section is an interesting energy gap we found in pure Fe simulations. Simulations were made for one 5 Mpc distant source emitting iron nuclei with discrete energy of 100, 200, 300, 400, 500 and 1000 EeV. The distribution of mass number on the Earth of the most energetic particles ( $E^{\text{Earth}} > 50$  EeV) is manifested for individual energies of the source in Figure 4.18 for the source distant 5 Mpc. The plot shows that with a higher energy of the source the final atomic number of particles hitting the Earth decreases. At the highest energy of the source 1000 EeV, all the particles on Earth with energy  $> 50$  EeV are either  ${}^4\text{He}$  or lighter. If we take into account also particles with lower energies than 50 EeV, the final composition is even lighter.

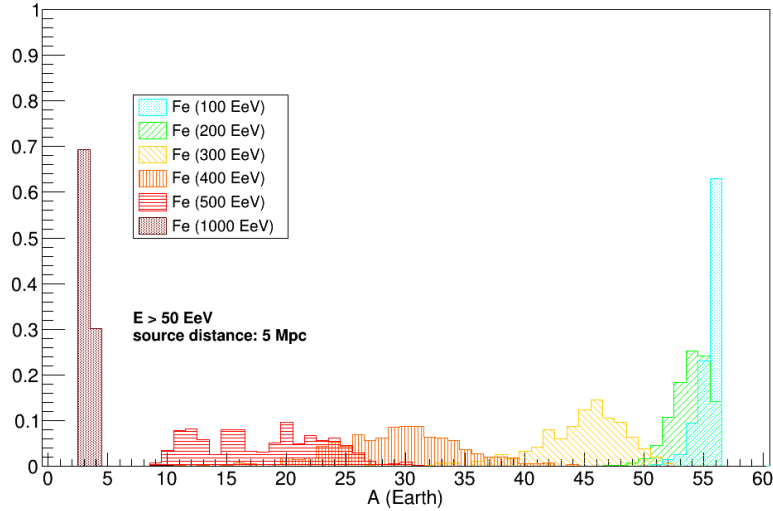


Figure 4.18: Distribution of the atomic number of the particles hitting the Earth with energy  $E_{\text{Earth}} > 50$  EeV. The source emitting iron nuclei was placed in the distance of 5 Mpc for different energies of the source (colours).

It is also interesting to look at the energy distribution of these particles on the Earth (see Figure 4.19). Three primary energies of the source were chosen (200, 300 and 400 EeV). In this figure we can notice a significant energy gap between the energies  $\approx (30 - 70)$  EeV for  $E_{\text{Source}} = 400$  EeV and  $\approx (30 - 140)$  EeV for lower energies of the source. If we investigate the atomic number of these particles we find that the atomic number distribution follows a similar shape of the distribution and while particles in the low energetic area are light nuclei, the high energetic particles over the gap are heavy nuclei. This behaviour is shown for the case of primary energy  $E_{\text{Source}} = 300$  EeV in Figure 4.20 where the particles with energies below the gap are drawn in blue and the particles with energies over the gap are drawn in red. Such distribution of atomic number suggests that such effect is caused by the photodisintegration of the Fe nuclei. In Figure 4.21 this energy gap is visualised for distances of the source from 1 Mpc to 10 Mpc. In all of these distances the energy gap is still visible even though it is slowly fading. For a source emitting iron nuclei with discrete energy, the energy gap does not fade away completely even for the distance of 50 Mpc for all energies. In the case of a source distant 50 Mpc, all the primary Fe with  $E_{\text{Source}} = 400$  EeV turn into light particles, but for  $E_{\text{Source}} = 200$  EeV and  $E_{\text{Source}} = 300$  EeV, the energy gap is still visible only it shifts towards lower energies as can be seen in Figure 4.22.

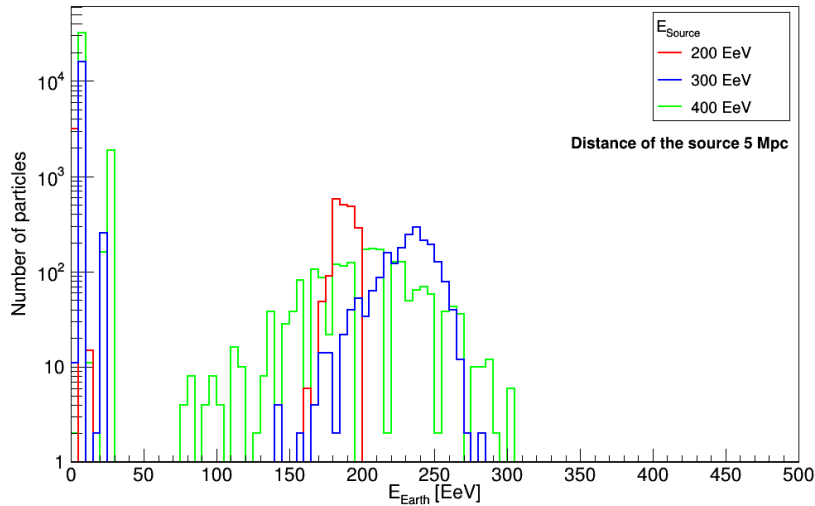


Figure 4.19: Energy distribution of the particles hitting the Earth from a source in the distance 5 Mpc emitting iron nuclei with energies 200 EeV, 300 EeV and 400 EeV.

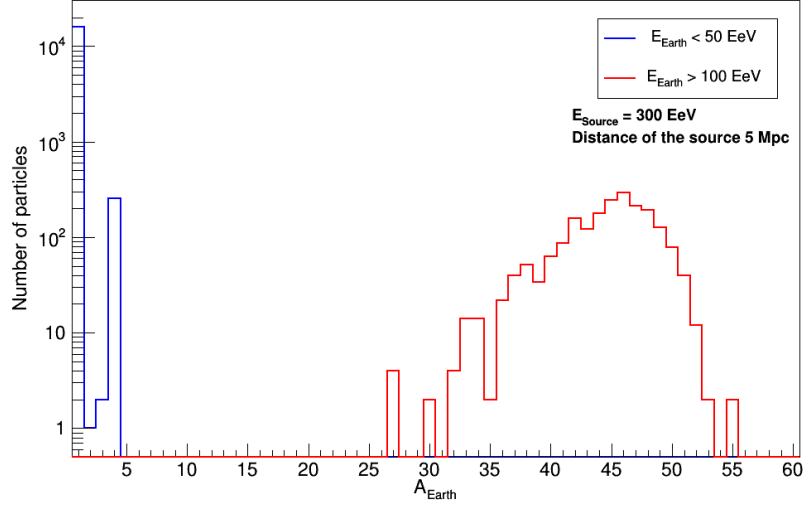


Figure 4.20: Distribution of the atomic number of particles hitting the Earth from a source in the distance 5 Mpc emitting iron nuclei with energy 300 EeV. Particles with energies  $E_{\text{Earth}} < 50$  EeV are drawn in blue, particles with energies  $E_{\text{Earth}} > 100$  EeV are drawn in red.

If we look on more realistic case, a source emitting particles with power law energy spectrum, the gap in the energy spectrum on the Earth is not visible any more. A simulation was made for a source in distance 5 Mpc with power law injection energy spectrum with spectral index 2 from the minimal energy  $E_{\text{min}}^{\text{Source}} = 1$  EeV up to the maximal rigidity  $R_{\text{max}}^{\text{Source}} = 10$  EeV emitting 10 000 iron nuclei. Energy distribution of particles hitting the Earth is shown in Figure 4.23. The energy gap vanished in the case of power law spectra, but some specific signature might be found with more sophisticated methods considering the mass of observed particles. This will be studied in future research.

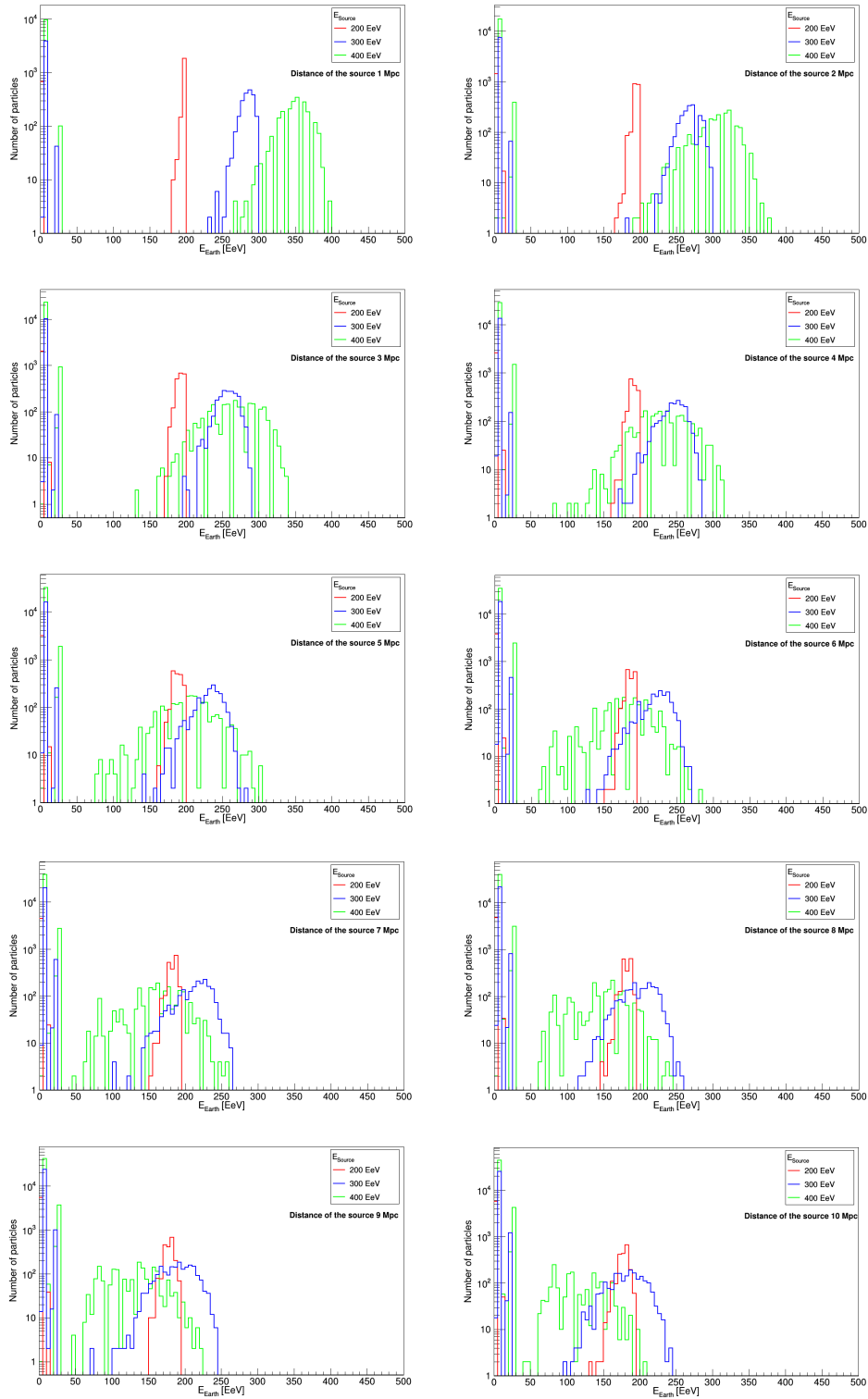


Figure 4.21: Energy distribution of the particles hitting the Earth from a source in the distance (1-10) Mpc emitting iron nuclei with energies 200 EeV, 300 EeV and 400 EeV.

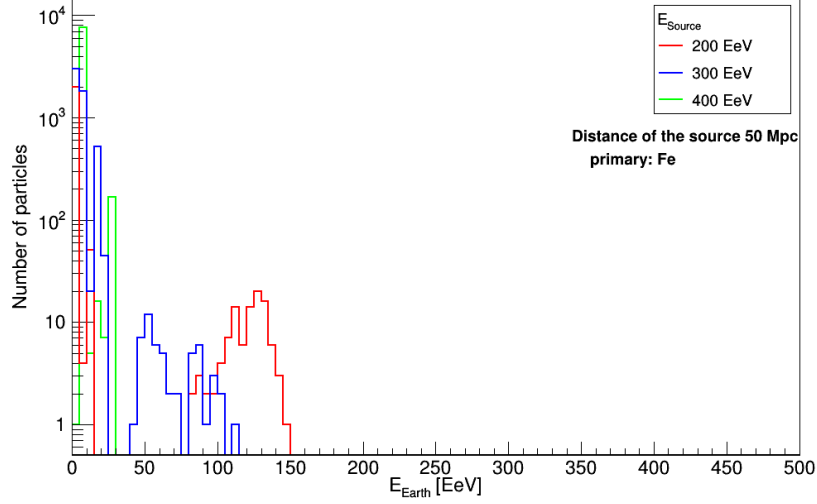


Figure 4.22: Energy distribution of the particles hitting the Earth from a source in the distance 50 Mpc emitting iron nuclei with energies 200 EeV, 300 EeV and 400 EeV.

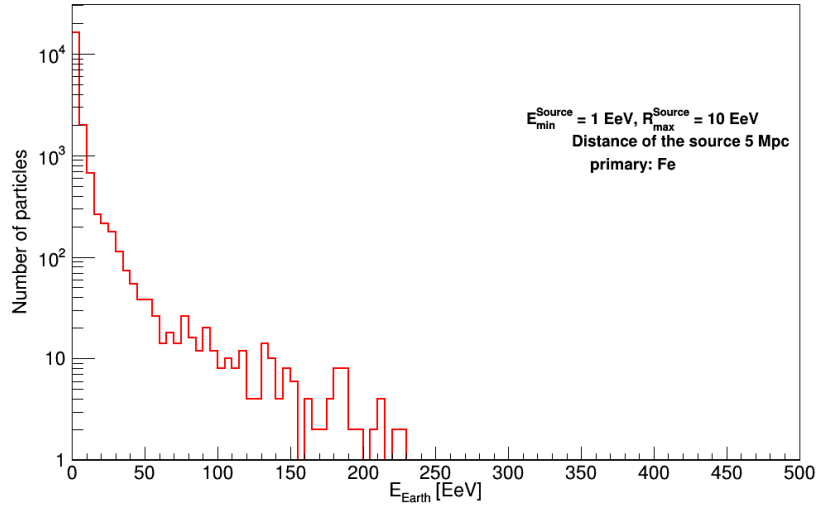


Figure 4.23: Energy distribution of the particles hitting the Earth from a source in the distance 5 Mpc emitting iron nuclei with power law injection energy spectrum with spectral index 2 from the minimal energy  $E_{min}^{Source} = 1$  EeV up to the maximal rigidity  $R_{max}^{Source} = 10$  EeV.

# Chapter 5

## Conclusions

The basic properties of cosmic-ray spectrum and its mass composition detected on the Earth were introduced together with the energy losses that particles undergo during their propagation in the Universe. A brief description of the Pierre Auger Observatory and different reconstruction techniques of the air showers were given. The main part of this work is devoted to the mass composition analysis of the Pierre Auger Observatory data and processing of the simulated data of cosmic-ray propagation in the Universe performed in CRPropa 3.

In the first part of Chapter 4, the shower universality was utilized in the reconstruction of the data measured by the Pierre Auger Observatory with the surface detector array.

Than the mean values of shower maximum ( $X_{\max}$ ) could be obtained from the SD data at energies  $E > 10^{19}$  eV. The universality reconstruction provides lower values of the mean  $X_{\max}$  than the classical hybrid reconstruction but both show a similar trend of the mass spectrum becoming heavier at the highest energies.

In the second part of Chapter 4, we analysed simulations of cosmic-ray propagation that were generated in CRPropa3 in one-dimensional space where deflections by galactic and extragalactic magnetic fields were not considered. We studied the energy loss lengths of different primary particles for different interactions on CMB as well as the energy evolution of the injected particles from the source to the observer. Our results indicate that the sources of the most energetic events (about  $10^{20}$  eV) should be closer than  $\sim 50$  Mpc and even closer for sources emitting heavier primaries. In the case of a source emitting iron nuclei, we would be able to observe a particle with energy higher than  $10^{20}$  eV only if the source was closer than 20 Mpc.

In the last part of this research work the focus was given to the fraction of observed helium nuclei on the Earth and a gap in the energy spectrum on

Earth caused by the discrete injection energy at the source of heavy primaries.

The He fractions higher than 20% were found to be very difficult to observe at the highest energies, where some models of hadronic interactions indicate interpreting the Pierre Auger data. The gap in the energy spectrum around  $\sim 50$  EeV for discrete injection energy at multiple distances of the source is most likely caused by the photodisintegrations of the emitted nuclei. Although this energy is not visible in the case of power law energy spectrum at the source, it might still be distinguished in more detailed investigation of the atomic number distribution of the particles hitting the Earth. This phenomena will be further studied in more detail.

In the future research we will move to the three-dimensional simulations where both galactic and extragalactic magnetic fields will be implemented to predict the mass composition and energy spectrum on Earth in the case of multiple sources and different initial conditions, such as injection energies, source distribution or mass composition at the source.

# Bibliography

- [1] D.H. Perkins. *Particle Astrophysics*. Oxford Master Series in Physics, 2009.
- [2] The Pierre Auger Collaboration. The Pierre Auger Cosmic Ray Observatory. *Nuclear Instruments and Methods in Physics Research*, 798:172–213, 2015.
- [3] H. Kawai, S. Yoshida, H. Yoshii, K. Tanaka, et al. Telescope Array Experiment. *Nuclear Physics B Proceedings Supplements*, 175:221–226, January 2008.
- [4] M. Bertolotti. *Celestial Messengers: Cosmic Rays: The Story of a Scientific Adventure*. 2013.
- [5] M. Unger, G. R. Farrar, and L. A. Anchordoqui. Origin of the ankle in the ultrahigh energy cosmic ray spectrum, and of the extragalactic protons below it. *Physical Review D*, 92(12):123001, December 2015.
- [6] KASCADE-Grande Collaboration - A. Haungs, W. D. Apel, and A. F. Badae. Investigating the 2nd knee: The KASCADE-Grande experiment. *ArXiv Astrophysics e-prints* : astro – ph/0508286, August 2005.
- [7] T. Abu-Zayyad, K. Belov, D. J. Bird, J. Boyer, et al. Measurement of the Cosmic-Ray Energy Spectrum and Composition from  $10^{17}$  to  $10^{18.3}$  eV Using a Hybrid Technique. *The Astrophysical Journal*, 557:686–699, August 2001.
- [8] K. Greisen. End to the cosmic-ray spectrum? *Phys. Rev. Lett.*, 16:748–750, April 1966.
- [9] G. T. Zatsepin and V. A. Kuz'min. Upper Limit of the Spectrum of Cosmic Rays. *Soviet Journal of Experimental and Theoretical Physics Letters*, 4:78, August 1966.

- [10] J. Blümer and Pierre Auger Collaboration. The northern site of the Pierre Auger Observatory. *New Journal of Physics*, 12(3):035001, March 2010.
- [11] T. Pierog, I. Karpenko, J. M. Katzy, E. Yatsenko, and K. Werner. EPOS LHC : test of collective hadronization with LHC data. *Physical Review C*, 92(1), September 2015.
- [12] S. Ostapchenko. Monte Carlo treatment of hadronic interactions in enhanced Pomeron scheme: QGSJET-II model. *Physical Review D*, 83(1):014018, January 2011.
- [13] E. J. Ahn, R. Engel, T. K. Gaisser, P. Lipari, and T. Stanev. Cosmic ray interaction event generator sibyll 2.1. *Physical Review D*, 80:094003, November 2009.
- [14] The Pierre Auger Collaboration. Muons in air showers at the Pierre Auger Observatory: Measurement of atmospheric production depth. *Physical Review D*, 90(1):012012, July 2014.
- [15] J. Bellido for "Pierre Auger Collaboration. Depth of maximum of air-shower profiles at the pierre auger observatory: Measurements above  $10^{17.2}$  ev and composition implications. In *Proceedings of Science*, volume 506, July 2017.
- [16] D. Kuempel. Extragalactic Propagation of Ultra-High Energy Cosmic Rays. *ArXiv e-prints* : 1409.3129, September 2014.
- [17] D. Allard. Propagation of extragalactic ultra-high energy cosmic-ray nuclei : implications for the observed spectrum and composition. *ArXiv e-prints* : 0906.3156, June 2009.
- [18] R. Alves Batista, D. Boncioli, A. di Matteo, A. van Vliet, and D. Walz. Effects of uncertainties in simulations of extragalactic UHECR propagation, using CRPropa and SimProp. *Journal of Cosmology and Astroparticle Physics*, 10:063, 2015.
- [19] R. M. Baltrusaitis, R. Cady, G. L. Cassiday, R. Cooperv, J. W. Elbert, P. R. Gerhardy, S. Ko, E. C. Loh, M. Salamon, D. Steck, and P. Sokol-sky. The Utah Fly's Eye detector. *Nuclear Instruments and Methods in Physics Research A*, 240:410–428, October 1985.
- [20] The Pierre Auger Collaboration, J. Abraham, P. Abreu, M. Aglietta, C. Aguirre, E. J. Ahn, D. Allard, I. Allekotte, J. Allen, P. Allison, and

- et al. The Fluorescence Detector of the Pierre Auger Observatory. *ArXiv e-prints*:0907.4282, July 2009.
- [21] T. K. Gaisser and A. M. Hillas. Reliability of the method of constant intensity cuts for reconstructing the average development of vertical showers. *International Cosmic Ray Conference*, 8:353–357, 1977.
- [22] K. Kamata and J. Nishimura. The Lateral and the Angular Structure Functions of Electron Showers. *Progress of Theoretical Physics Supplement*, 6:93–155, 1958.
- [23] K. Greisen. *The extensive air showers, Progress in Cosmic Ray Physics Vol. III*. 1956.
- [24] J. Hersil, I. Escobar, D. Scott, G. Clark, and S. Olbert. The Lateral and the Angular Structure Functions of Electron Showers. *Physical Review Letters*, 6, 1961.
- [25] M. Ave, M. Roth, and A. Schulz. A generalized description of the time dependent signals in extensive air shower detectors and its applications. *Astroparticle Physics*, 88:46–59, February 2017.
- [26] M. Ave, R. Engel, M. Roth, and A. Schulz. A generalized description of the signal size in extensive air shower detectors and its applications. *Astroparticle Physics*, 87:23–39, 2017.
- [27] R. Alves Batista, A. Dundovic, M. Erdmann, K.-H. Kampert, D. Kuempel, G. Müller, G. Sigl, A. van Vliet, D. Walz, and T. Winchen. CR-Propa 3-a public astrophysical simulation framework for propagating extraterrestrial ultra-high energy particles. *Journal of Cosmology and Astroparticle Physics*, 5:038, May 2016.
- [28] A. Domínguez et al. Extragalactic background light inferred from AEGIS galaxy-SED-type fractions. *Monthly Notices of the Royal Astronomical Society*, 410:2556–2578, February 2011.
- [29] R. Alves Batista, M. Erdmann, C. Evoli, K.-H. Kampert, D. Kuempel, G. Müller, G. Sigl, A. van Vliet, D. Walz, and T. Winchen. CRPropa: A public framework to propagate UHECRs in the universe. volume 99 of *European Physical Journal Web of Conferences*, page 13004, August 2015.
- [30] R. Jansson and G. R. Farrar. A New Model of the Galactic Magnetic Field. *The Astrophysical Journal*, 757:14, September 2012.

- [31] M. S. Pshirkov, P. G. Tinyakov, P. P. Kronberg, and K. J. Newton-McGee. Deriving the Global Structure of the Galactic Magnetic Field from Faraday Rotation Measures of Extragalactic Sources. *The Astrophysical Journal*, 738:192, September 2011.
- [32] R. Aloisio, D. Boncioli, A. F. Grillo, S. Petrerá, and F. Salamida. SimProp: a simulation code for ultra high energy cosmic ray propagation. *Journal of Cosmology and Astroparticle Physics*, 10:007, October 2012.
- [33] D. N. Spergel et al. First-year wilkinson microwave anisotropy probe (wmap) observations: Determination of cosmological parameters. *The Astrophysical Journal Supplement Series*, 148(1):175, 2003.
- [34] Observer Team. The auger observer. <http://augerobserver.fzk.de>.
- [35] Cuts for karlsruhe universality. <https://web.ikp.kit.edu/augeroracle/doku.php?id=auger:observer>, September 2016. [Online; 7/9/2017].
- [36] Pierre Auger Collaboration. Interpretation of the depths of maximum of extensive air showers measured by the Pierre Auger Observatory. *Journal of Cosmology and Astroparticle Physics*, 2:026, February 2013.
- [37] Xmax moments and composition fractions - icrc 2017. <https://www.auger.unam.mx/AugerWiki/XmaxHeatIcrc2017>, September 2017. [Online; 13/9/2017].
- [38] The Pierre Auger Collaboration. Depth of maximum of air-shower profiles at the Pierre Auger Observatory. I. Measurements at energies above  $10^{17.8}$  eV. *Physical Review D*, 90(12):122005, December 2014.
- [39] M. De Domenico, M. Settimo, S. Riggi, and E. Bertin. Reinterpreting the development of extensive air showers initiated by nuclei and photons. *Journal of Cosmology and Astroparticle Physics*, 7:050, July 2013.
- [40] D. J. Bird et al. Evidence for correlated changes in the spectrum and composition of cosmic rays at extremely high-energies. *Physical Review Letters*, 71:3401–3404, 1993.